Coupling compositional gas liquid Darcy and free gas flows at porous and free flow domains interface

Roland Masson, L Trenty, Yumeng Zhang

Coupling compositional gas liquid Darcy and free gas flows at porous and free flow domains interface

R. Masson[*], L. Trenty[†], Y. Zhang[‡]

June 11, 2016

Abstract

This paper proposes an efficient splitting algorithm to solve coupled liquid gas Darcy and free gas flows at the interface between a porous medium and a free-flow domain. This model is compared to the reduced model introduced in [6] using a 1D approximation of the gas free flow. For that purpose, the gas molar fraction diffusive flux at the interface in the free-flow domain is approximated by a two point flux approximation based on a low-frequency diagonal approximation of a Steklov-Poincaré type operator. The splitting algorithm and the reduced model are applied in particular to the modelling of the mass exchanges at the interface between the storage and the ventilation galleries in radioactive waste deposits.

1 Introduction

Flow and transport processes in domains composed of a porous medium and an adjacent free-flow region appear in a wide range of applications. It includes for example, industrial drying applications such as the production of building materials, food processing, and wood and paper production, or also, environmental applications such as land-atmospheric interaction and soil evaporation and evapotranspiration. In this article we will focus on the design of efficient algorithms to simulate the mass exchanges at the interface between the porous and free-flow regions, assuming a fixed temperature in the porous and free-flow domains. The effect of the vaporization on the temperature is neglected and will be considered in a future work. Typically in drying processes, the porous medium initially saturated with the liquid phase is dried by suction in the neighbourhood of the interface between the porous and free-flow domains. The gas phase penetrates the porous domain and the liquid phase is vaporized in the free-flow domain. In this work, our focus is not only on the drying of the porous medium but also on the evolution of the gas composition in the free-flow region. This is motivated by our main interest for such models to the prediction of the mass exchanges occurring at the interface between the radioactive waste deep geological repositories and the ventilation excavated galleries. In this application, the ventilation galleries must be proved to remain safe during the entire period of reversibility of the storage fixed to 100 years in France by the national savety authorities.

To model such physical processes, one needs to account in the porous medium for the flow of the liquid and gas phases including the vaporization of the water component in the gas phase and the dissolution of the gaseous components in the liquid phase. In the free-flow region, a single phase gas

[*]Laboratoire de Mathématiques J.A. Dieudonné, UMR 7351 CNRS, University Nice Sophia Antipolis, and team COFFEE, INRIA Sophia Antipolis Méditerranée, Parc Valrose 06108 Nice Cedex 02, France, roland.masson@unice.fr

[†]Andra, 1-7 rue Jean Monnet 92290 Chatenay-Malabry, France, laurent.trenty@andra.fr

[‡]Laboratoire de Mathématiques J.A. Dieudonné, UMR 7351 CNRS, University Nice Sophia Antipolis, and team COFFEE, INRIA Sophia Antipolis Méditerranée, Parc Valrose 06108 Nice Cedex 02, France, yumeng.zhang@unice.fr

free flow is considered assuming that the liquid phase is instantaneously vaporized at the interface. This gas free flow has to be compositional to account for the change of the relative humidity in the free-flow region which has a strong feedback on the liquid flow rate at the interface.

If many works have been performed to model and discretize the coupling of single phase Darcy and free flows (see the review [14]), there are much fewer works on the coupling of a two phase liquid gas compositional Darcy flow with a single phase compositional gas free flow. Such a coupled model has been recently proposed in [24, 3] using matching conditions at the interface between the porous-medium and the free-flow regions. These coupling conditions state the continuity of the molar normal flux of each component taking into account the instantaneous vaporization of the liquid phase, the continuity of the gas molar fractions, and the liquid gas thermodynamical equilibrium. In our case, the Beavers-Joseph condition [4] used in [24, 3] is replaced by a no slip condition due to the low permeability of the porous medium.

The main objective of this article is to design an efficient algorithm to solve this coupled problem. Sequential algorithms based on Dirichlet-Neumann boundary conditions at the interface (see [12, 10] and the review [11]) are frequently used for solving drying problems. As mentioned in [12, 10], the stability of sequential algorithms requires very small time steps at the scale of the free flow leading to very large CPU times. In order to obtain an efficient algorithm, one needs to be able to use time steps at the scale of the porous medium with a quasi-stationary computation of the free flow at each time step. For this purpose, fully coupled algorithms such as the ones developed in [3, 17, 23] have been introduced, but they lead to non-linear and linear systems which are difficult and expensive to solve since they do not take advantage of the different levels of coupling in the non-linear system. Alternatively in [27], for a related but different problem coupling the Richards equation in the porous medium and the Stokes equation for the liquid phase in the free flow region, the authors introduce a splitting algorithm using a small time step in the free-flow region and a large time step in the porous medium.

The algorithm developed in this article is based on a splitting between the strongly and weakly coupled equations and unknowns of the full system. It can be used either as a fixed point algorithm leading to the fully coupled solution at convergence or simply as a sequential algorithm which will be shown to provide a sufficient accuracy compared with the fully coupled solution. Our choice of the splitting of the full system is based on the physical understanding of the strong and weak couplings in the system. On the one hand, the water molar fraction in the free-flow region is strongly coupled to the liquid pressure and liquid flux at the porous and free-flow domains interface due to the liquid gas thermodynamical equilibrium. On the other hand, the gas velocity perturbation in the free-flow domain, which is induced by the coupling with the porous medium, is small compared with the forced convection velocity. Consequently, it has a weak feedback on the porous medium. Therefore, the idea of our splitting strategy is to solve, in a first step, the porous-medium equations coupled to the convection-diffusion equations for the gas molar fractions in the free-flow domain at fixed velocity and pressure in the free-flow domain. Then, the total molar normal flux at the interface is computed and used in the second step of the algorithm to compute the velocity and pressure in the free-flow domain solving the Navier-Stokes equations. This splitting strategy allows to use a time step in both domains at the time scale of the porous medium. Compared with fully coupled approaches, it leads to simpler and smaller linear and non-linear systems to be solved at each time step with the possibility to use the best available algorithm for each subproblem separately.

The second objective of this paper is to improve the reduced model introduced in [6] based on a 1D approximation of the flow in the free-flow domain. It is motivated by the large longitudinal dimension of the ventilation galleries compared with their diameter allowing to reduce the model in the gallery to a 1D free flow. In the spirit of Convective Mass Transfer Coefficients CMTCs (see the

review [11] and the references therein for a discussion about CMTCs), the model includes on the free-flow side a Two Point Flux Approximation (TPFA) of the diffusion fluxes for the gas molar fractions at the interface. In [6], the practical computation of the TPFA transmissibility at the interface is not discussed and just said to be related to the convection-diffusion boundary layer thickness in the free-flow domain.

In this article, a model is proposed to compute this boundary layer thickness parameter or equivalently the TPFA transmissibility for the diffusion flux. It plays an essential role in the reduced model in order to obtain a good approximation of the liquid evaporation rate at the interface since it concentrates at the interface all the information on the free-flow velocity and diffusivity. In the framework of drying problems, the recent review [11] provides a discussion about CMTCs which are usually obtained using empirical correlations with the gas velocity not taking into account their spatial variations nor the complexity of the free-flow domain geometry. They are also often obtained by an analogy with Convective Heat Transfer Coefficients which is not always valid (see the comments in [11]). In this article, the computation of the boundary layer thickness parameter will be based on a diagonal low-frequency approximation of a Steklov-Poincaré type operator for the stationary convection-diffusion equation at fixed velocity. It will lead to a boundary layer thickness depending on the position $\mathbf{x}$ at the interface. In addition, our computation will take into account the coupling with the 1D free flow in the gallery avoiding the use of a fixed reference gas molar fraction as it is the case for CMTCs (see [11]).

In order to assess the efficiency of the splitting algorithm and the accuracy of the reduced model, a simple 2D setting exhibited in Figure 2 is used. In the porous medium Ω^p, we consider a compositional liquid gas Darcy flow using the phase pressures and component fugacities formulation introduced in [22]. In the free-flow domain Ω^g, the turbulent nature of the flow is taken into account using an algebraic model leading to the computation of a mean turbulent profile. This longitudinal mean turbulent profile is defined as a stationary solution of the RANS model (Reynolds Averaged Navier-Stokes, see e.g. [7, 5]) without the coupling with the porous-medium flow. Then, this mean turbulent profile $\mathbf{u}_t$ provides the turbulent dynamic viscosity μ_t and the turbulent diffusivity D_t that are used to compute the velocity, pressure and gas molar fraction in Ω^g solving the RANS compositional model at fixed turbulent viscosity μ_t and diffusivity D_t. The turbulent viscosity and diffusivity can be fixed thanks to the small perturbation of the velocity and pressure induced by the coupling in the free-flow region. Note also that the turbulent diffusivity D_t plays an essential role in the liquid evaporation rate at the interface.

The 2D domain is discretized using a Cartesian mesh conforming at the interface and refined on both sides of the interface Γ in order to take into account the viscous boundary layer on the gallery side and the strong liquid pressure gradient on the porous-medium side. The space discretization uses a Marker-And-Cell (MAC) scheme for the RANS model [16] and a cell centered finite volume scheme for the Darcy flow in Ω^p and for the convection-diffusion equations in Ω^g. In both cases, the diffusion fluxes (Darcy and turbulent diffusion terms) are approximated by a TPFA and the convection numerical fluxes are obtained by a first order upwind scheme. The time integration uses an implicit Euler scheme. Three test cases are considered. The first two test cases are defined by Andra using data set from lab experiments and in accordance with the deep disposal center for French radioactive waste project. These two test cases couple a very low permeable porous medium with either a horizontal or a vertical gallery. The third test case considers the convective drying of a porous medium with a much larger permeability.

The outline of the paper is the following. In Section 2, the formulation of the coupled model is introduced using the phase pressures and component fugacities formulation in the porous medium. Then, the splitting algorithm is described. In Section 3 the reduced model using a 1D model in

the free-flow domain is described as well as the computation of the gas molar fraction boundary layer thickness. In Section 4, the 2D setting for our numerical experiments is detailed as well as the discretization in the porous medium and in the gallery. Then, the results of the three test cases are presented and discussed.

2 Formulation of the coupled model and splitting algorithm

Let Ω^p denote the porous-medium domain and Ω^g the free-flow domain. The interface between the two domains is denoted by $\Gamma = \partial\Omega^p \cap \partial\Omega^g$.

In the following, the boundary conditions at the external boundary $\partial\Omega^g \setminus \Gamma$ of the free-flow domain are considered to be independent on time to simplify the presentation. Since our model is at the time scale of the porous medium, a quasi-stationary RANS model detailed below is used to describe the mean turbulent flow in the free-flow domain. Hence, the dependence on time of the gas velocity, pressure and molar fraction in the free-flow domain is only induced by the coupling with the porous medium.

The following physical assumptions are used in order to simplify the mathematical formulation of the coupled model and prepare the splitting algorithm. The coupling with the porous medium is basically assumed to induce a small perturbation of the free-flow gas velocity, pressure, and molar fraction. Hence, in the free-flow domain, the gas molar and mass densities can be assumed to be fixed. Also, we can defined an independent on time uncoupled mean turbulent flow denoted by $(\mathbf{u}_t, p_t)$ corresponding to the stationary solution of the RANS model obtained with a zero normal velocity at the interface Γ. In our application, it means that we impose $\mathbf{u}_t = 0$ at the interface Γ since a no slip velocity rather than the Beavers-Joseph condition is used thanks to the low permeability of the porous medium. The turbulent closure used for the computation of the uncoupled flow $(\mathbf{u}_t, p_t)$ defines a turbulent viscosity denoted by $\mu_t(\mathbf{x})$ from which can be obtained the turbulent diffusivity denoted by $D_t(\mathbf{x})$. Using the small perturbation assumption, it is assumed that the same turbulent viscosity and diffusivity can be used in order to compute the coupled flow and transport RANS model in the free-flow domain.

2.1 Formulation of the coupled model

Let $\alpha \in \{g, l\}$ denote the gas and liquid phases assumed to be both defined by a mixture of components $i \in \mathcal{C}$ among which the water component denoted by e which can vaporize in the gas phase, and a set of gaseous components $j \in \mathcal{C} \setminus \{e\}$ which can dissolve in the liquid phase. The model is assumed to be isothermal with a fixed temperature T_e. Following [22], the liquid gas Darcy flow formulation uses the gas pressure p^g, the liquid pressure p^l, and the component fugacities $f = (f_i)_{i\in\mathcal{C}}$ as primary unknowns, denoted by $\mathcal{U} = (p^g, p^l, f)$ in the following. In this formulation, following [19], the component molar fractions $c^\alpha = (c_i^\alpha)_{i\in\mathcal{C}}$ of each phase $\alpha \in \{g, l\}$ are the functions $c_i^\alpha(\mathcal{U})$ of $\mathcal{U}$ defined by inversion of the equations $f_i^\alpha(c^\alpha, p^g, p^l) = f_i$, $i \in \mathcal{C}$, where f_i^α is the fugacity of the component i in the phase α. In addition, for $\alpha \in \{g, l\}$, the phase pressure p^α is extended in the absence of the phase in such a way that the closure law $\sum_{i\in\mathcal{C}} c_i^\alpha(\mathcal{U}) = 1$ is always imposed (see [22]). The phase molar and mass densities, as well as the phase viscosities are denoted in the following by respectively $\zeta^\alpha(p^\alpha, c^\alpha)$, $\rho^\alpha(p^\alpha, c^\alpha)$, $\mu^\alpha(p^\alpha, c^\alpha)$ for $\alpha \in \{g, l\}$. For the sake of simplicity, for $\xi = \zeta^\alpha$, ρ^α, or μ^α, we will use the notation $\xi(\mathcal{U})$ for the function $\xi(p^\alpha, c^\alpha(\mathcal{U}))$.
Finally, we define the liquid saturation as the function $\mathcal{S}^l(\mathbf{x}, p^g - p^l)$ of $p_c = p^g - p^l$ defined by the inverse of the monotone graph extension of the capillary pressure function $p_c(\mathbf{x}, .)$, and we set $\mathcal{S}^g(\mathbf{x}, .) = 1 - \mathcal{S}^l(\mathbf{x}, .)$ (see [22]). This leads to the following set of equations for the unknowns $\mathcal{U}$ in

the porous medium

$$\left\{\begin{array}{ll} \phi\partial_t n_i(\mathbf{x},\mathcal{U}) + \mathrm{div}\,(\mathbf{V}_i) = 0,\ i\in\mathcal{C} & \text{on } \Omega^p\times(0,T),\\ \mathbf{V}_i = \displaystyle\sum_{\alpha\in\{g,l\}} -m_i^\alpha(\mathbf{x},\mathcal{U})\mathbf{K}\Big(\nabla p^\alpha - \rho^\alpha(\mathcal{U})\mathbf{g}\Big),\ i\in\mathcal{C} & \text{on } \Omega^p\times(0,T),\\ \displaystyle\sum_{i\in\mathcal{C}} c_i^\alpha(\mathcal{U}) = 1,\ \alpha\in\{g,l\} & \text{on } \Omega^p\times(0,T), \end{array}\right. \tag{1}$$

with the number of mole of the component i per unit pore volume defined by

$$n_i(\mathbf{x},\mathcal{U}) = \sum_{\alpha\in\{g,l\}} c_i^\alpha(\mathcal{U})\zeta^\alpha(\mathcal{U})\mathcal{S}^\alpha(\mathbf{x},p^g-p^l),$$

and the mobility of the component i in phase α defined by

$$m_i^\alpha(\mathbf{x},\mathcal{U}) = c_i^\alpha(\mathcal{U})\zeta^\alpha(\mathcal{U})\frac{k_r^\alpha(\mathbf{x},\mathcal{S}^\alpha(\mathbf{x},p^g-p^l))}{\mu^\alpha(\mathcal{U})}.$$

In the free-flow domain, let us first define the uncoupled mean turbulent flow as the solution $(\mathbf{u}_t, p_t)$ of the following stationary RANS model

$$\left\{\begin{array}{r} \rho^g\mathrm{div}\Big(\mathbf{u}_t\otimes\mathbf{u}_t\Big) + \mathrm{div}\Big(-(\mu^g+\mu_t)\left(\nabla\mathbf{u}_t+\nabla^t\mathbf{u}_t\right)\Big) + \nabla p_t = \rho^g\mathbf{g} \text{ on } \Omega^g,\\ \mathrm{div}\,(\mathbf{u}_t) = 0 \text{ on } \Omega^g, \end{array}\right. \tag{2}$$

with boundary condition $\mathbf{u}_t = 0$ at the interface Γ. In (2), μ_t is the turbulent viscosity which is modelled e.g. using an algebraic turbulent model or a more advanced $k-\epsilon$ model. Note that the turbulent viscosity μ_t vanishes at the interface Γ but is much larger than μ^g away from the viscous boundary layer. This turbulent flow is responsible for a turbulent diffusivity denoted by D_t and typically given by $D_t = \dfrac{1}{S_c}\dfrac{\mu_t}{\rho^g}$ where S_c is the Schmidt number (see e.g. [5]). This turbulent diffusivity, which is much larger than D^g away from the viscous boundary layer, plays an essential role in the order of magnitude of the evaporation rate.

The coupling of the free flow with the porous-medium flow leads to the new RANS gas velocity $\mathbf{u}$, pressure p, and gas molar fraction c. Let us denote the velocity and pressure corrections with respect to the uncoupled flow by $\tilde{\mathbf{u}} = \mathbf{u} - \mathbf{u}_t$ and $\tilde{p} = p - p_t$. Due to our small perturbation assumption, the densities can be assumed to be fixed and the turbulent viscosity μ_t and diffusivity D_t can be set to be the functions of $\mathbf{x}$ provided by the uncoupled flow $(\mathbf{u}_t,\, p_t)$. Hence, it results that $(\tilde{\mathbf{u}},\tilde{p},c)$ are solutions of the following RANS compositional model

$$\left\{\begin{array}{ll} \rho^g\mathrm{div}\Big(\mathbf{u}_t\otimes\tilde{\mathbf{u}}+\tilde{\mathbf{u}}\otimes\mathbf{u}_t+\tilde{\mathbf{u}}\otimes\tilde{\mathbf{u}}\Big) & \\ \qquad -\mathrm{div}\Big((\mu^g+\mu_t)\left(\nabla\tilde{\mathbf{u}}+\nabla^t\tilde{\mathbf{u}}\right)\Big) + \nabla\tilde{p} = 0 & \text{on } \Omega^g\times(0,T),\\ \partial_t c_i + \mathrm{div}\,(\mathbf{F}_i) = 0, i\in\mathcal{C} & \text{on } \Omega^g\times(0,T),\\ \mathbf{F}_i = c_i\mathbf{u} - (D^g+D_t)\nabla c_i, i\in\mathcal{C} & \text{on } \Omega^g\times(0,T),\\ \displaystyle\sum_{i\in\mathcal{C}} c_i = 1 & \text{on } \Omega^g\times(0,T). \end{array}\right. \tag{3}$$

Note that in (3) the component molar conservations in the free-flow domain are kept transient only in order to ease the non-linear solution of the coupled system at the start of the simulation.

At the interface Γ between the free-flow domain and the porous medium, the coupling conditions are an adaptation to those stated in [24]. As already stated, the Beavers-Joseph condition at the

interface Γ is replaced by a no slip condition due to the low permeability of the porous medium in our application. The remaining conditions are the continuity of the molar normal flux for each component $i \in \mathcal{C}$ assuming that the liquid phase is instantaneously vaporized, the continuity of the gas molar fractions, the continuity of the normal component of the normal stress, and the liquid gas thermodynamical equilibrium. We obtain the following interface conditions

$$\begin{cases} \mathbf{V}_i \cdot \mathbf{n} = \zeta^g \mathbf{F}_i \cdot \mathbf{n},\ i \in \mathcal{C} & \text{on } \Gamma \times (0,T), \\ c_i^g(\mathcal{U}) = c_i, i \in \mathcal{C} & \text{on } \Gamma \times (0,T), \\ p^g = p + \mathbf{n} \cdot \Big(\rho^g \mathbf{u} \otimes \mathbf{u} - \mu^g(\nabla \mathbf{u} + \nabla^t \mathbf{u})\Big)\mathbf{n} & \text{on } \Gamma \times (0,T), \\ \displaystyle\sum_{i \in \mathcal{C}} c_i^\alpha(\mathcal{U}) = 1,\ \alpha \in \{g,l\} & \text{on } \Gamma \times (0,T), \\ \mathbf{u} \wedge \mathbf{n} = 0 & \text{on } \Gamma \times (0,T), \end{cases} \tag{4}$$

where $\mathbf{n}$ denotes the unit normal vector at the interface Γ oriented outward of the porous-medium domain.

2.2 Splitting algorithm

In [3, 17, 23] the Darcy and free-flow unknowns corresponding in our case to $\mathcal{U}$, $\mathbf{u}$, p and c are solved using a monolithic Newton algorithm at each time step of a fully implicit Euler time integration scheme. Given the complexity of the full system, this approach naturally leads to difficulties in solving the non-linear and linearized systems.

Alternatively, many coupling strategies simply rely on a sequential coupling algorithm of Dirichlet-Neumann type using typically two different codes for the Darcy and free flows. This type of sequential coupling algorithm leads to very small time steps due to the strong coupling between the liquid pressure p^l and the water molar fraction c_e at the interface Γ which is induced by the thermodynamical equilibrium. For example, in [12, 10], a time step of 0.1 s is reported resulting in roughly 100h of CPU time for a few days of simulation. We refer to [11] for a recent review including a list of codes implementing sequential or fully implicit coupling algorithms for the modelling of drying processes at the interface between a porous medium and a free-flow domain.

Our approach is rather to split the system in two simpler subsystems at each time step of the fully implicit Euler time integration scheme. In a first step, for given $\mathbf{u}$ and p in Ω^g, the strongly coupled unknowns $\mathcal{U}$ in Ω^p, c in Ω^g, and $(\mathbf{u}\cdot\mathbf{n})$ at Γ are computed using a Newton algorithm solving the Darcy flow in the porous medium together with the convection-diffusion equations in the free-flow domain and part of the interface conditions. The gas velocity $\mathbf{u}$ and gas pressure p in Ω^g are then computed in a second step solving the momentum and divergence free equations using step 1 normal velocity $(\mathbf{u}\cdot\mathbf{n})$ at the interface Γ. The two steps 1 and 2 are iterated, as a fixed point algorithm for the normal velocity $(\mathbf{u}\cdot\mathbf{n})$ at the interface Γ, until the stopping criteria $\|1 - \sum_{i\in\mathcal{C}} c_i\|_{L^\infty(\Omega^g)} \leq \epsilon$ is satisfied for a given accuracy ϵ. The convergence of this fixed point method is expected to be fast due to the weak dependence of the unknowns $\mathcal{U}$, c, and $(\mathbf{u}\cdot\mathbf{n})$ on the velocity and pressure perturbations $\tilde{\mathbf{u}}$ and $\tilde{p}$. We will see in the numerical Section 4 that, in practice, the sequential version of this algorithm, i.e. a single fixed point iteration, suffices to obtain an accurate result. Since the linear and nonlinear systems of step 1 and step 2 subproblems are smaller and easier to solve separately than the fully coupled systems, it results that our splitting algorithm is more efficient than fully coupled algorithms.

We detail below the two steps of the splitting algorithm at a given time step Δt^n between times t^{n-1} and t^n, which are iterated until convergence of the gas molar fractions such that $\|1 - \sum_{i\in\mathcal{C}} c_i\|_{L^\infty(\Omega^g)} \leq \epsilon$. An Euler implicit time integration is used in both domains. The unknowns at

time t^n are denoted with the n superscript. The fixed point iteration count is denoted by k and the splitting algorithm is initialized with the solution from the previous time step.

Step 1: it computes $\mathcal{U}^{n,k}$ in the porous medium, $c^{n,k}$ in the free-flow domain and $(\mathbf{u}\cdot\mathbf{n})^{n,k}$ at the interface, at fixed velocity $\mathbf{u}^{n,k-1}$ and pressure $p^{n,k-1}$ in the free-flow domain, as the solution of the system coupling the Darcy flow model

$$\left\{\begin{array}{ll} \phi\dfrac{n_i(\mathbf{x},\mathcal{U}^{n,k})-n_i(\mathbf{x},\mathcal{U}^{n-1})}{\Delta t^n}+\mathrm{div}\left(\mathbf{V}_i^{n,k}\right)=0,\ i\in\mathcal{C} & \text{on } \Omega^p,\\ \mathbf{V}_i^{n,k}=\displaystyle\sum_{\alpha\in\{g,l\}}-m_i^\alpha(\mathbf{x},\mathcal{U}^{n,k})\mathbf{K}\Big(\nabla p^{\alpha,n,k}-\rho^\alpha(\mathcal{U}^{n,k})\mathbf{g}\Big),\ i\in\mathcal{C} & \text{on } \Omega^p,\\ \displaystyle\sum_{i\in\mathcal{C}}c_i^\alpha(\mathcal{U}^{n,k})=1,\ \alpha\in\{g,l\} & \text{on } \Omega^p, \end{array}\right. \tag{5}$$

with the convection-diffusion equations in the free-flow domain

$$\left\{\begin{array}{ll} \dfrac{c_i^{n,k}-c_i^{n-1}}{\Delta t^n}+\mathrm{div}\left(\mathbf{F}_i^{n,k}\right)=0,\ i\in\mathcal{C} & \text{on } \Omega^g,\\ \mathbf{F}_i^{n,k}=c_i^{n,k}\mathbf{u}^{n,k-1}-(D^g+D_t)\nabla c_i^{n,k},\ i\in\mathcal{C} & \text{on } \Omega^g,\\ \mathbf{F}_i^{n,k}\cdot\mathbf{n}=c_i^{n,k}(\mathbf{u}\cdot\mathbf{n})^{n,k}-D^g\nabla c_i^{n,k}\cdot\mathbf{n},\ i\in\mathcal{C} & \text{on } \Gamma. \end{array}\right. \tag{6}$$

and the following subset of the interface conditions

$$\left\{\begin{array}{ll} \mathbf{V}_i^{n,k}\cdot\mathbf{n}=\zeta^g\mathbf{F}_i^{n,k}\cdot\mathbf{n},\ i\in\mathcal{C} & \text{on } \Gamma,\\ c_i^g(\mathcal{U}^{n,k})=c_i^{n,k},\ i\in\mathcal{C} & \text{on } \Gamma,\\ p^{g,n,k}=p^{n,k-1}+\mathbf{n}\cdot\Big(\rho^g\mathbf{u}^{n,k-1}\otimes\mathbf{u}^{n,k-1}-\mu^g(\nabla\mathbf{u}^{n,k-1}+\nabla^t\mathbf{u}^{n,k-1})\Big)\mathbf{n} & \text{on } \Gamma,\\ \displaystyle\sum_{i\in\mathcal{C}}c_i^\alpha(\mathcal{U}^{n,k})=1,\ \alpha\in\{g,l\} & \text{on } \Gamma. \end{array}\right. \tag{7}$$

Note that in (6) and (7), the normal gas velocity $(\mathbf{u}\cdot\mathbf{n})^{n,k}$ is used for the convection flux at the interface Γ and not $\mathbf{u}^{n,k-1}\cdot\mathbf{n}$. Note also that, in (6), the conservative correction of the normal flux at the interface Γ is to be understood as a correction at the discrete level. To be rigorous at the continuous level, one would need to use a non conservative formulation. Both choices are equivalent at convergence and we found that the first choice was more efficient.

Step 2: Given the normal gas velocity $(\mathbf{u}\cdot\mathbf{n})^{n,k}$ at the interface Γ computed at step 1, step 2 computes the gas velocity $\mathbf{u}^{n,k}=\mathbf{u}_t+\tilde{\mathbf{u}}^{n,k}$ and the gas pressure $p^{n,k}=p_t+\tilde{p}^{n,k}$ as the solution at time t^n of the following RANS model

$$\left\{\begin{array}{ll} \rho^g\mathrm{div}\Big(\mathbf{u}_t\otimes\tilde{\mathbf{u}}^{n,k}+\tilde{\mathbf{u}}^{n,k}\otimes\mathbf{u}_t+\tilde{\mathbf{u}}^{n,k}\otimes\tilde{\mathbf{u}}^{n,k}\Big) & \\ \qquad -\mathrm{div}\Big((\mu^g+\mu_t)(\nabla\tilde{\mathbf{u}}^{n,k}+\nabla^t\tilde{\mathbf{u}}^{n,k})\Big)+\nabla\tilde{p}^{n,k}=0 & \text{on } \Omega^g,\\ \mathrm{div}(\tilde{\mathbf{u}}^{n,k})=0 & \text{on } \Omega^g,\\ \mathbf{u}^{n,k}\cdot\mathbf{n}=(\mathbf{u}\cdot\mathbf{n})^{n,k} & \text{on } \Gamma. \end{array}\right. \tag{8}$$

3 Reduced model

In this section, the free-flow domain Ω^g is assumed, to simplify the notations, to be the cylindrical domain $(0,L)\times S$ of length L and of section S with S an open simply connected subdomain of $\mathbb{R}^2$.

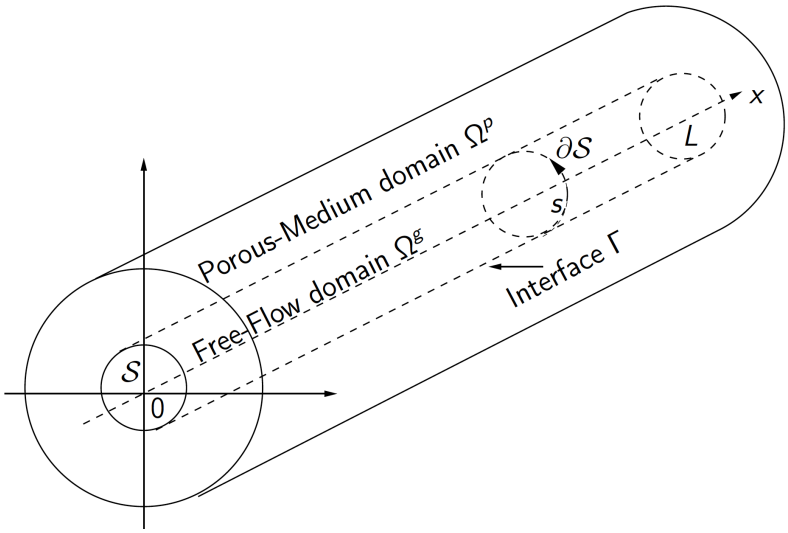

Figure 1: Example of reduced model geometry exhibiting the cylindrical free-flow domain Ω^g of section S and lengh L, the porous-medium domain Ω^p, and the interface Γ. The curvilinear coordinate along ∂S is denoted by s.

The porous medium Ω^p shares the interface $\Gamma = (0, L) \times \partial S$ with the free-flow domain Ω^g. The curvilinear coordinate along ∂S is denoted by s (see Figure 1). The extension of what follows to more complex free-flow domains in diffeomorphism with a cylindrical domain is straightforward.

Assuming L large compared to the diameter of the section S, a reduced model has been introduced in [6] using a 1D approximation of the free-flow and transport model. The good approximation properties of this reduced model rely crucially on the choice of the transmissibility $\frac{D^g}{\delta(\mathbf{x})}$ at the interface Γ. This transmissibility is used to approximate by a TPFA the diffusion fluxes for the gas molar fractions in the free-flow domain at the interface Γ. In [6], the practical computation of δ is not discussed and just said to be related to the convection-diffusion boundary layer thickness in the free-flow domain. In this section, the reduced model of [6] is briefly recalled in subsection 3.1. Then, subsection 3.2 introduces a model to compute $\delta(\mathbf{x})$. The role of $\delta(\mathbf{x})$ is to concentrate at the interface Γ the convection diffusion operator in the free-flow domain i.e. all the information about the turbulent velocity and diffusivity. It will be shown to be exactly the definition of a Steklov-Poincaré type operator. Since the exact Steklov-Poincaré operator is time dependent and also non local, the practical definition of δ will be based on (i) an independent on time approximation of the convection-diffusion operator, and (ii) on a diagonal low-frequency approximation of the Steklov-Poincaré operator related to this approximate convection-diffusion operator.

3.1 Reduced 1D model in the free-flow domain

The reduced model uses in the free-flow domain, the following mean values in the section S depending on the longitudinal coordinate x and on time t: the pressure p, the longitudinal velocity u, and the gas molar fraction c. At the interface Γ, the gas molar fraction cannot be approximated by the section mean value c due to the convection-diffusion boundary layer. It is given by the gas molar fraction on the porous medium side $c^g(\mathcal{U})$ from the gas molar fraction continuity at the interface. The gas pressure jump at the interface can be neglected due to the small gas viscosity and to the small flow rate between the porous medium and the free-flow domain. It results that the free-flow pressure p of the reduced model can be approximated by the porous medium pressure p^g at the interface. The last unknown of the reduced model is the normal gas velocity at the interface Γ as a

function of $\mathbf{x} \in \Gamma$ and time t. This normal velocity is denoted by $(\mathbf{u} \cdot \mathbf{n})$ with the normal oriented outward of the porous medium.

The reduced model system amounts to find the porous-medium unknowns $\mathcal{U}(\mathbf{x}, t)$ on $\Omega^p \times (0, T)$, and the free-flow domain unknowns $u(x, t)$, $p(x, t)$, $c(x, t)$ on $(0, L)\times(0, T)$ and $(\mathbf{u}\cdot\mathbf{n})(\mathbf{x}, t)$ on $\Gamma\times(0, T)$ satisfying the Darcy flow system (1), the following conservation equations along the free-flow domain

$$\begin{cases} \partial_t c_i + \partial_x(c_i u) = \dfrac{1}{|S|\zeta^g} \displaystyle\int_{\partial S} \mathbf{V}_i \cdot \mathbf{n} \, ds, \; i \in \mathcal{C} \text{ on } (0, L) \times (0, T), \\ \displaystyle\sum_{i\in\mathcal{C}} c_i = 1 \text{ on } (0, L) \times (0, T), \\ -\partial_x p = f_{pd}(u) \text{ on } (0, L) \times (0, T), \end{cases} \tag{9}$$

coupled with the following modified system at the interface Γ

$$\begin{cases} \mathbf{V}_i \cdot \mathbf{n} = \zeta^g \Big(c_i^g(\mathcal{U})(\mathbf{u} \cdot \mathbf{n})^+ + c_i(\mathbf{u} \cdot \mathbf{n})^- + \dfrac{D^g}{\delta}(c_i^g(\mathcal{U}) - c_i) \Big), \; i \in \mathcal{C} \text{ on } \Gamma \times (0, T), \\ \displaystyle\sum_{i\in\mathcal{C}} c_i^\alpha(\mathcal{U}) = 1, \; \alpha \in \{g, l\} \text{ on } \Gamma \times (0, T), \\ p^g = p, \text{ on } \Gamma \times (0, T), \end{cases} \tag{10}$$

In (10), the notation $a^+ = \max(a, 0)$ and $a^- = \min(a, 0)$ has been used. The first interface condition in (10) accounts for the normal flux continuity of each component $i \in \mathcal{C}$ using a TPFA of the convection-diffusion flux in the free-flow domain. The approximation of the convection flux is based on an upwinding of the gas molar fraction between its value $c^g(\mathcal{U})$ at the interface and its mean value c. The TPFA of the diffusion flux is obtained using the transmissibility $\frac{D^g}{\delta}$ which is discussed in the next subsection.

The function f_{pd} is the pressure drop model, which is typically given by $f_{pd}(u) = (\alpha_g u + \beta_g |u| u)$ with $\alpha_g \geq 0$ and $\beta_g \geq 0$, $\alpha_g + \beta_g > 0$. In our application, due to the small gas viscosity, this pressure drop can be neglected. We refer to [6] for a more detailed explanation of the reduced model.

3.2 Molar fraction boundary layer thickness model

The computation of the boundary layer thickness δ is related to the TPFA of the diffusion flux at the interface Γ. It is clear that a linear approximation of the gas molar fraction in the normal direction will be wrong since it does not take into account the boundary layer related to the convection-diffusion operator.

The derivation of our model is first based on an approximation of the convection-diffusion operator $\partial_t + \operatorname{div}\Big((\mathbf{u}_t + \tilde{\mathbf{u}}) - (D^g + D_t)\nabla\Big)$ in order to eliminate the time dependent terms. The time derivative can be neglected since we consider the porous medium time scale. The time dependent velocity perturbation $\tilde{\mathbf{u}}$ is small compared with the diffusion term in the viscous boundary layer and it is also small compared with $\mathbf{u}_t$ away from the boundary layer. Consequently it can also be neglected and we introduce the stationary convection-diffusion operator $\mathcal{L}$ defined for all $d \in H^1(\Omega^g)$ by

$$\mathcal{L}d = \operatorname{div}\Big(\mathbf{u}_t d - (D^g + D_t)\nabla d\Big),$$

recalling that $\operatorname{div}(\mathbf{u}_t) = 0$ on Ω^g and that $\mathbf{u}_t = 0$ and $D_t = 0$ on Γ. We define the solution d of the following stationary convection-diffusion equation given a constant boundary condition $d_{\text{in}} \in \mathbb{R}$ on $\Gamma^g_{\text{in}} = \{0\} \times S$ and a boundary condition $d_\Gamma \in H^{\frac{1}{2}}(\Gamma)$ on Γ:

$$\begin{cases} \mathcal{L}d = 0 & \text{on } \Omega^g, \\ d = d_\Gamma & \text{on } \Gamma, \\ d = d_{\text{in}} & \text{on } \Gamma^g_{\text{in}}, \\ \nabla d \cdot \mathbf{n} = 0 & \text{on } \Gamma^g_{\text{out}} = \{L\} \times S. \end{cases} \tag{11}$$

Let us denote by $\mathcal{S}_P$ the linear Steklov-Poincaré operator such that for all $d_\Gamma \in H^{\frac{1}{2}}(\Gamma)$

$$\mathcal{S}_P(d_\Gamma - d_{\text{in}}) = -\nabla d \cdot \mathbf{n} \in H^{-\frac{1}{2}}(\Gamma),$$

and let us denote by M the linear compact operator from $H^{\frac{1}{2}}(\Gamma)$ to $H^{\frac{1}{2}}(\Gamma)$ such that for all $d_\Gamma \in H^{\frac{1}{2}}(\Gamma)$

$$M(d_\Gamma - d_{\text{in}}) = \frac{1}{|S|}\int_S d(.,y,z)dydz - d_{\text{in}}.$$

Let us denote by 1_Γ the function equal to 1 on Γ. Then, we define for $d_{\text{in}} \in \mathbb{R}$, $d_\Gamma = d_\gamma 1_\Gamma$ with $d_\gamma \in \mathbb{R}$, $d_{\text{in}} \neq d_\gamma$,

$$\delta = \frac{d_\Gamma - \frac{1}{|S|}\int_S d(.,y,z)dydz}{-\nabla d \cdot \mathbf{n}} = \frac{(I-M)1_\Gamma}{\mathcal{S}_P 1_\Gamma}$$

This definition of δ is clearly independent on the choice of both d_γ and d_{in}. Also from the maximum principle, $\delta(\mathbf{x}) > 0$ for all $\mathbf{x} \in \Gamma$.

From the maximum principle and the Fredholm alternative, the linear operator $I - M$ defines a bijection from $H^{\frac{1}{2}}(\Gamma)$ to $H^{\frac{1}{2}}(\Gamma)$. Hence we can define the operator

$$\overline{\mathcal{S}}_P = \mathcal{S}_P(I-M)^{-1},$$

which relates the normal flux at Γ to the difference between the trace on Γ and the section mean values as follows

$$-\nabla d \cdot \mathbf{n} = \overline{\mathcal{S}}_P\Big(d_\Gamma - \frac{1}{|S|}\int_S d(.,y,z)dydz\Big).$$

In this framework, $\dfrac{1}{\delta}$ clearly appears as a diagonal approximation of the operator $\overline{\mathcal{S}}_P$ which is built to be exact for constant boundary conditions on Γ.

It is more usual to relate the flux to the difference between the trace of the gas molar fraction on Γ and a reference gas molar fraction corresponding in our case to d_{in}. With our approach, it will lead to the diagonal approximation $\frac{D^g}{\delta} = D^g \mathcal{S}_P 1_\Gamma$ of the operator $D^g \mathcal{S}_P$. Our definition has the advantage to take into account the coupling of the interface conditions with the 1D gas free flow and avoid the use of a reference gas molar fraction.

3.3 Splitting algorithm for the reduced model

Considering the small size of the 1D free-flow model compared with the porous medium model, the solution of the reduced model at each time step can be obtained as in [6] using a Newton algorithm to solve the fully coupled system. In the following numerical experiments it was more convenient to use the splitting algorithm of subsection 2.2 which is easily adapted to the reduced model as follows.

Step 1: it computes $\mathcal{U}^{n,k}$ in the porous medium, $c^{n,k}$ in the 1D free-flow domain and $(\mathbf{u}\cdot\mathbf{n})^{n,k}$ at the interface, at fixed velocity $u^{n,k-1}$ and pressure $p^{n,k-1}$ in the 1D free-flow domain, as the solution of the system coupling the Darcy flow system (5), with the following 1D convection-diffusion equations in the free-flow domain

$$\frac{c_i^{n,k} - c_i^{n-1}}{\Delta t^n} + \partial_x\left(c_i^{n,k} u^{n,k-1}\right) = \frac{1}{|S|\zeta^g}\int_{\partial S} \mathbf{V}_i^{n,k}\cdot\mathbf{n}\, ds,\ i \in \mathcal{C} \text{ on } (0,L), \tag{12}$$

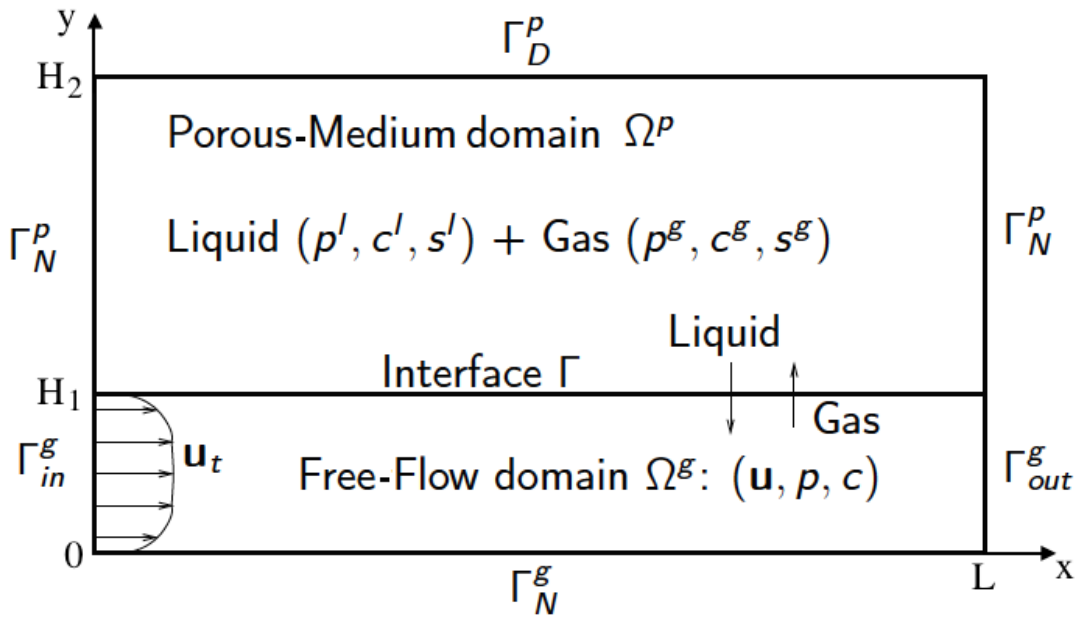

Figure 2: Free-flow domain Ω^g, porous-medium domain Ω^p, interface Γ, and remaining boundaries for our 2D test case.

and the following subset of the interface conditions

$$\begin{cases} \mathbf{V}_i^{n,k} \cdot \mathbf{n} = \zeta^g \Big(c_i^g(\mathcal{U}^{n,k})((\mathbf{u}\cdot\mathbf{n})^{n,k})^+ + c_i^{n,k}((\mathbf{u}\cdot\mathbf{n})^{n,k})^- + \dfrac{D^g}{\delta}(c_i^g(\mathcal{U}^{n,k}) - c_i^{n,k}) \Big),\ i \in \mathcal{C} \text{ on } \Gamma, \\ \displaystyle\sum_{i\in\mathcal{C}} c_i^\alpha(\mathcal{U}^{n,k}) = 1,\ \alpha \in \{g, l\} \text{ on } \Gamma, \\ p^{g,n,k} = p^{n,k} \text{ on } \Gamma. \end{cases} \tag{13}$$

Step 2: Given the Darcy fluxes at the interface $V_i^{n,k}$, $i \in \mathcal{C}$ computed at step 1, step 2 computes the gas velocity $u^{n,k}$ and the gas pressure $p^{n,k}$ as the solution at time t^n of the following 1D elliptic (for p) model

$$\begin{cases} \partial_x u^{n,k} = \dfrac{1}{|S|\zeta^g} \displaystyle\int_{\partial S} \sum_{i\in\mathcal{C}} \mathbf{V}_i^{n,k} \cdot \mathbf{n}\ ds,\ i \in \mathcal{C} \text{ on } (0, L), \\ -\partial_x p^{n,k} = f_{pd}(u^{n,k}) \text{ on } (0, L). \end{cases} \tag{14}$$

4 Numerical tests

In order to assess the efficiency of the splitting algorithm and to compare the full and reduced models, we consider in the following tests a simple 2D setting with $\Omega^g = (0, L)\times(0, H_1)$, $\Omega^p = (0, L)\times(H_1, H_2)$ and $\Gamma = (0, L)\times\{H_1\}$. Figure 2 exhibits the two domains, the interface Γ and the external boundaries Γ_D^p, Γ_N^p, Γ_{in}^g, Γ_{out}^g, and Γ_N^g. We consider the set of components $\mathcal{C} = \{e, a\}$ where e denotes the water component, and a the gaseous air component with the fixed Henry constant $H_a = 6\cdot 10^9$ Pa. The gas molar density is given by $\zeta^g(p^g) = \frac{p^g}{RT_e}$ mol.m^{-3}, and the liquid molar density is fixed to $\zeta^l = 55555$ mol.m^{-3}. The phase viscosities are fixed to $\mu^g = 18.51\cdot 10^{-6}$ Pa.s and $\mu^l = 10^{-3}$ Pa.s. The mass densities are defined by $\rho^\alpha = \zeta^\alpha \sum_{i\in\mathcal{C}} c_i^\alpha M_i$ with the molar masses of the components $M_a = 29\cdot 10^{-3}$ Kg.mol^{-1}, $M_e = 18\cdot 10^{-3}$ Kg.mol^{-1}.

The fugacities of the components in the gas phase are given by Dalton's law for an ideal mixture of perfect gas $f_i^g = c_i^g p^g$, $i \in \mathcal{C}$. The fugacities of the components in the liquid phase are given by

Henry's law for the dissolution of the air component in the liquid phase $f_a^l = c_a^l H_a$, and by Raoult-Kelvin's law for the water component in the liquid phase $f_e^l = c_e^l P_{sat}(T_e)\exp\Big(\frac{-(p^g-p^l)}{\zeta^l R T_e}\Big)$, where $P_{sat}(T_e)$ is the vapour pressure of the pure water.

The solution of the equation $f^\alpha(c^\alpha, p^g, p^l) = f$ leads to the following component molar fractions c_i^α as functions of $\mathcal{U}$:

$$\left\{\begin{array}{ll} c_e^l(\mathcal{U}) = \dfrac{f_e}{P_{sat}(T_e)}\exp\Big(\dfrac{(p^g-p^l)}{\zeta^l R T_e}\Big), & c_a^l(\mathcal{U}) = \dfrac{f_a}{H_a}, \\ c_e^g(\mathcal{U}) = \dfrac{f_e}{p^g}, & c_a^g(\mathcal{U}) = \dfrac{f_a}{p^g}. \end{array}\right. \tag{15}$$

The relative permeabilities and capillary pressure in the porous medium are given by the following van Genuchten laws

$$k_r^l(s^l) = \left\{\begin{array}{ll} 0 & \text{if } \ s^l < s_r^l, \\ 1 & \text{if } \ s^l > 1 - s_r^g, \\ \sqrt{\bar{s}^l}\Big(1-(1-(\bar{s}^l)^{1/m})^m\Big)^2 & \text{if } \ s_r^l \le s^l \le 1 - s_r^g, \end{array}\right.$$

$$k_r^g(s^g) = \left\{\begin{array}{ll} 0 & \text{if } \ s^g < s_r^g, \\ 1 & \text{if } \ s^g > 1 - s_r^l, \\ \sqrt{1-\bar{s}^l}\Big(1-(\bar{s}^l)^{1/m}\Big)^{2m} & \text{if } \ s_r^g \le s^g \le 1 - s_r^l, \end{array}\right.$$

and

$$s^l(-p_c) = s_r^l + (1 - s_r^l - s_r^g)\frac{1}{\Big(1+(\frac{p_c}{P_r})^n\Big)^m},$$

with

$$\bar{s}^l = \frac{s^l - s_r^l}{1 - s_r^l - s_r^g}.$$

In our numerical tests, the mean turbulent velocity $\mathbf{u}_t(y)$ is longitudinal and defined by the mean turbulent profile $u_t(y)$ with $\mathbf{u}_t(y) = \begin{pmatrix} u_t(y) \\ 0 \end{pmatrix}$. This mean turbulent profile is obtained using the following Prandtl algebraic turbulent model for the turbulent viscosity (see [30, 7, 5])

$$\mu_t = \rho^g (l_m(y))^2 |u_t'(y)|, \ \ l_m(y) = 0.41 \min(y, H_1 - y).$$

Using this turbulent closure, the RANS model (2) for $(\mathbf{u}_t, p_t)$ amounts to compute the solution (u_t, p_t) of the system

$$\left\{\begin{array}{ll} \partial_y\Big(-(\mu^g + \mu_t)\partial_y u_t\Big) + \partial_x p_t = 0 & \text{on } \Omega^g, \\ \partial_y p_t = -\rho^g g & \text{on } \Omega^g, \end{array}\right. \tag{16}$$

which reduces to the following Ordinary Differential Equation (ODE) for $u_t(y)$

$$\Big(\mu^g + \rho^g (l_m(y))^2 |u_t'|\Big) u_t' = \alpha_t (H_1/2 - y),$$

to be integrated between $y = 0$ and $y = \frac{H_1}{2}$ by symmetry. The integration constant of this ODE and the constant α_t are obtained using the conditions $u_t(0) = 0$ and

$$\frac{1}{H_1}\int_0^{H_1} u_t(y)dy = w_{\text{in}},$$

where w_{in} is the prescribed mean value of the input velocity. Using the outflow boundary condition (17) specified below, the turbulent pressure is defined by

$$p_t(x,y) = p_{\text{out}} - \rho^g g y - \alpha_t(x-L),$$

where p_{out} is the outflow pressure for $y=0$, and $g = 9.81 m.s^{-2}$ is the gravity acceleration. In our numerical tests, the turbulent diffusivity is related to the turbulent viscosity by

$$D_t(y) = \frac{\mu_t(y)}{\rho^g},$$

corresponding to a Schmidt number of 1.

The porous medium is initially saturated by the liquid phase with imposed pressure p^l_{init} and composition $c^l_{a,init} = 0$, $c^l_{e,init} = 1$ which combined with the equation $c^g_e(\mathcal{U}_{\text{init}}) + c^g_a(\mathcal{U}_{\text{init}}) = 1$ defines the initial unknowns $\mathcal{U}_{\text{init}}$. At the top porous-medium boundary Γ^p_D, a Dirichlet boundary condition is imposed equal to the initial condition $\mathcal{U}_D = \mathcal{U}_{\text{init}}$. At both sides Γ^p_N of the porous medium, a zero normal flux boundary condition is imposed for all components. The initial condition in the free-flow domain is given by $p_{\text{init}} = 10^5$ Pa and $c_{e,init} = 1 - c_{a,init}$ defined by the prescribed relative humidity

$$H_{r,init} = \frac{c_{e,init} p_{\text{init}}}{P_{sat}(T_e)}.$$

At the boundary Γ^g_{in}, the input molar fractions are set to $c_{\text{in}} = c_{\text{init}}$, and the mean turbulent profile $\mathbf{u}_t(y)$ is imposed. At the boundary Γ^g_{out}, the following outflow boundary conditions are imposed

$$p - (\mu^g + \mu_t(y))\partial_x u = p^{\text{out}} - \rho^g g y, \quad \partial_x v = 0, \tag{17}$$

with $p_{\text{out}} = p_{\text{init}}$. The usual gradient is used in this outflow condition rather than the symmetric gradient in such a way that this condition can be satisfied by $(\mathbf{u}_t, p_t)$. The diffusion normal fluxes are set to zero for all components $i \in \mathcal{C}$ on Γ^g_{out}. At the bottom boundary Γ^g_N, the velocity $\mathbf{u}$ is set to zero as well as the diffusion normal fluxes for all components $i \in \mathcal{C}$.

4.1 Finite Volume Discretization on a Cartesian mesh

The domain $(0,L)\times(0,H_2)$ is discretized by a non-uniform Cartesian mesh refined at both sides of the interface Γ. The discretizations of the step 1 and step 2 of the splitting algorithm of subsection 2.2 are briefly described below and we refer to the PhD thesis of Yumeng Zhang [32] for a more detailed description.

TPFA discretization of Step 1: A finite volume cell centered discretization with a TPFA of the Darcy fluxes and a first order upwinding of the mobility terms is used for the porous-medium model (5). Let us refer to [26, 2] for details. The convection-diffusion equations (6) are discretized using as well a cell centered finite volume scheme with a TPFA of the diffusion fluxes and a first order upwinding of the convection terms. The discretization of step 1 is conservative in the sense that the same porous medium and convection-diffusion fluxes are used for the normal fluxes continuity equations of (7).

Let $\mathcal{M}^p$ (resp. $\mathcal{M}^g$) denotes the set of cells of Ω^p (resp. Ω^g). The set of edges of the interface Γ is denoted by $\mathcal{E}_\Gamma$. The set of discrete unknowns is defined by $\mathcal{U}_K = (p^g_K, p^l_K, f_K) \in \mathbb{R}^{\mathcal{C}}\times\mathbb{R}^2$, $K \in \mathcal{M}^p$ in the porous medium, by $c_K \in \mathbb{R}^{\mathcal{C}}$, $K \in \mathcal{M}^g$ in the free-flow domain, and by $\mathcal{U}_\sigma = (p^g_\sigma, p^l_\sigma, f_\sigma) \in \mathbb{R}^{\mathcal{C}}\times\mathbb{R}^2$ and $(\mathbf{u}\cdot\mathbf{n})_\sigma \in \mathbb{R}$ for all edges $\sigma \in \mathcal{E}_\Gamma$ at the interface where $(\mathbf{u}\cdot\mathbf{n})_\sigma$ is the normal gas velocity at the edge σ oriented outward of the free-flow domain.

Since at a given fixed point iteration, the molar fractions do not sum to 1, it is convenient to use the normalized molar fractions $\overline{c}_i = \frac{c_i}{\sum_{j\in\mathcal{C}} c_j}, i \in \mathcal{C}$ in the discretization of the fluxes at the interface

Γ. Using the interface conditions, this allows the following elimination of the normal velocity at the interface: $(\mathbf{u}\cdot\mathbf{n})_\sigma = \frac{1}{\zeta^g}\sum_{i\in\mathcal{C}}(\mathbf{V}_i\cdot\mathbf{n})_\sigma$.

The discrete coupled system at each time step n and at each fixed point iteration k is solved using a Newton algorithm. For all cells $K\in\mathcal{M}^p$ and for all edges $\sigma\in\mathcal{E}_\Gamma$, both fugacities f_e and f_a can be eliminated from the non-linear system using the closure equations $c_e^\alpha(\mathcal{U})+c_a^\alpha(\mathcal{U})=1$, $\alpha\in\{g,l\}$. Using these eliminations, and the elimination of the normal velocities $(\mathbf{u}\cdot\mathbf{n})_\sigma$ for $\sigma\in\mathcal{E}_\Gamma$, the Jacobian system to be solved at each Newton iteration reduces to Cardinal($\mathcal{C}$) equations and unknowns in each cell $K\in\mathcal{M}^p\cup\mathcal{M}^g$ and at each edge $\sigma\in\mathcal{E}_\Gamma$. This linear system is solved using the sequential version of the SuperLU direct sparse solver [20], [13].

MAC discretization of Step 2: A staggered MAC (Marker-And-Cell) scheme is used to discretize the RANS model (8) on the non uniform Cartesian mesh of the domain Ω^g. We refer to [16, 25, 31] for a detailed description. For the domain Ω^g, denoting by N_x the number of cells in the x direction and by N_y the number of cells in the y direction, the discrete unknowns of the staggered MAC discretization are the vertical edge normal velocity perturbations

$$\tilde{u}_{i+\frac{1}{2},j},\ i=0,\cdots,N_x,\ j=1,\cdots,N_y,$$

the horizontal edge normal velocities

$$v_{i,j+\frac{1}{2}}=\tilde{v}_{i,j+\frac{1}{2}},\ i=1,\cdots,N_x,\ j=0,\cdots,N_y,$$

and the cell centered pressure perturbations

$$\tilde{p}_{i,j},\ i=1,\cdots,N_x,\ j=1,\cdots,N_y.$$

The convection fluxes are discretized using a first order upwind approximation of the velocities. This discrete system is solved at each time step n and at each fixed point iteration k using a Quasi-Newton algorithm where the Jacobian matrix is approximated by dropping the non-linear part of the system. The main advantage of this approach is that this approximate Jacobian does not depend on n nor on k. Hence it is factorized only once using a direct sparse linear solver and a forward-backward sweep is performed at each Quasi-Newton iteration. In the numerical experiments the sequential version of the direct sparse solver SuperLU (see e.g.[13, 20]) is used.

Communications between step 1 and 2: Step 1 sends to step 2 the normal velocities $(\mathbf{u}\cdot\mathbf{n})^{k,n}_{\sigma(i)}$ at the interface where $\sigma(i)$ is the one to one mapping between $i=1,\cdots,N_x$ and the set of edges $\mathcal{E}_\Gamma$. Step 2 sends to step 1 the normal velocities at the gallery interior edges, as well as the pressure jumps at $\sigma(i)$, $i=1,\cdots,N_x$ which, in all our numerical experiments, are in practice negligible. In the following numerical experiments the non-linear stopping criteria are fixed to

- $\epsilon_{\text{Newton}}=10^{-7}$ for the relative l^2 norm of the residual of step 1 non-linear system,
- $\epsilon_{QuasiNewton}=10^{-6}$ for the relative l^2 norm of the difference between two successive Quasi-Newton iterates of the discrete RANS non-linear system,
- $\epsilon_{FixedPoint}=10^{-8}$ on $\|1-\sum_{i\in\mathcal{C}}c_i\|_{l^\infty}$ for the fixed point iterations of the coupled problem.

Let us mention that the reduced model is discretized using the same finite volume schemes adapted to the 1D model in the free-flow domain. The same Cartesian mesh than for the full dimensional model is used in the x direction in the free-flow domain and in both directions in the porous-medium domain.

4.2 Andra test case with a horizontal gallery

The setting of this test case is exhibited in Figure 3. The porous-medium domain $\Omega^p = (0, L) \times (H_1, H_2)$, with $H_1 = 5$ m and $H_2 = 15$ m, includes two rocktypes. The concrete rocktype in the domain $(0, L) \times (H_1, H_1 + 1)$ is defined by the van Genuchten parameters $n = 1.54$, $s_r^l = 0.01$, $s_r^g = 0$, $P_r = 2 \cdot 10^6$ Pa, the isotropic permeability $\mathbf{K} = 10^{-18}$ m^2 and the porosity $\phi = 0.3$. The Callovo Oxfordian (COx) clay rocktype in the domain $(0, L) \times (H_1 + 1, H_2)$ is defined by the van Genuchten parameters $n = 1.49$, $s_r^l = 0.4$, $s_r^g = 0$, $P_r = 15 \cdot 10^6$ Pa, the isotropic permeability $\mathbf{K} = 5 \cdot 10^{-20}$ m^2, and the porosity $\phi = 0.15$. The initial and top boundary liquid pressure in the porous medium is set to $p^l_{\text{init}} = 40 \cdot 10^5$ Pa, and the temperature is fixed to $T_e = 303$ K both in the porous medium and in the gallery. The initial and input relative humidity in the gallery is fixed to $H_{r,init} = 0.5$ and the ouput and initial pressure in the gallery to $p_{\text{init}} = p_{\text{out}} = 10^5$ Pa. In the following tests, we evaluate the influence of the input velocity w_{in} and of the length L of the gallery on the mean relative humidity in the gallery and on the mean evaporation rate at the interface. The input velocity w_{in} is set to 0.05, 0.5 or 5 m. s^{-1}, and the length L is set to 25, 100 or 400 m. The simulation is run over a period of 200 years, chosen large enough to reach the stationary state, and the time steps range from 1 s at the start of the simulation to 10 years at the end of the simulation with a total of 123 time steps (see Table 1). To assess the numerical convergence of the discrete solutions, a family of Cartesian meshes are tested with increasing sizes set to $N_x \times N_y = 25 \times 50$, 50×100, 100×200, and 200×400. All these meshes are uniform in the x direction and are refined in the direction y on both sides of the interface Γ as well as at the COx and concrete rocktypes interface $y = H_1 + 1$. The number of cells on both subdomains Ω^g and Ω^p is roughly the same. To fix ideas, the sizes of the first cells at both sides of the interface Γ are set to to δy_1 in the gallery side and to δy_2 in the porous-medium side with $(\delta y_1, \delta y_2)$ in meters equal to $(1.62 \cdot 10^{-2}, 6.95 \cdot 10^{-3})$, $(7.09 \cdot 10^{-3}, 3.06 \cdot 10^{-3})$, $(3.32 \cdot 10^{-3}, 1.44 \cdot 10^{-3})$, and $(1.61 \cdot 10^{-3}, 6.96 \cdot 10^{-4})$ for respectively the meshes 25×50, 50×100, 100×200, and 200×400. Note that, with these values of δy_1 on the gallery side, the meshes are refined down to the scale of the laminar boundary layer.

In order to understand the following numerical results, we need to have in mind the orders of magnitude at the interface Γ of the molar fractions which are such that $c_a^l \ll c_e^l$, $c_e^g \ll c_a^g$, $c_e \ll c_a$, and of the molar gas and liquid Darcy fluxes which are such that $|\mathbf{V}^g \cdot \mathbf{n}| \ll |\mathbf{V}^l \cdot \mathbf{n}|$. At the interface Γ, it follows from the normal fluxes continuity conditions (4) that the water component convection flux $\zeta^g c_e \mathbf{u} \cdot \mathbf{n}$ is small compared to the water component diffusion flux $-\zeta^g D^g \nabla c_e \cdot \mathbf{n}$ with a ratio roughly equal to c_e.

This can be checked numerically in Figure 4 plotting the mean water component convection and diffusion fluxes at the interface as a function of time. Using this remark, we can explain the shape of the mean evaporation rate at the interface as a function of time exhibited in Figure 6. It classically includes two stages characterized for the first stage by a roughly constant evaporation rate followed for the second stage by a decrease of the evaporation rate down to the stationary state. It is also known that the evaporation rate of the first stage weakly depends on the properties of the porous medium but the duration of the stage does depend on the porous-medium properties. This first stage actually corresponds to a value of the water component molar fraction c_e at the interface roughly equal to $\frac{P_{sat}(T_e)}{p_{\text{out}}}$ (relative humidity H_r equal to 1) due to a relatively large water influx in the gallery. Using this Dirichlet boundary condition and the previous remark, the value of the water influx can be

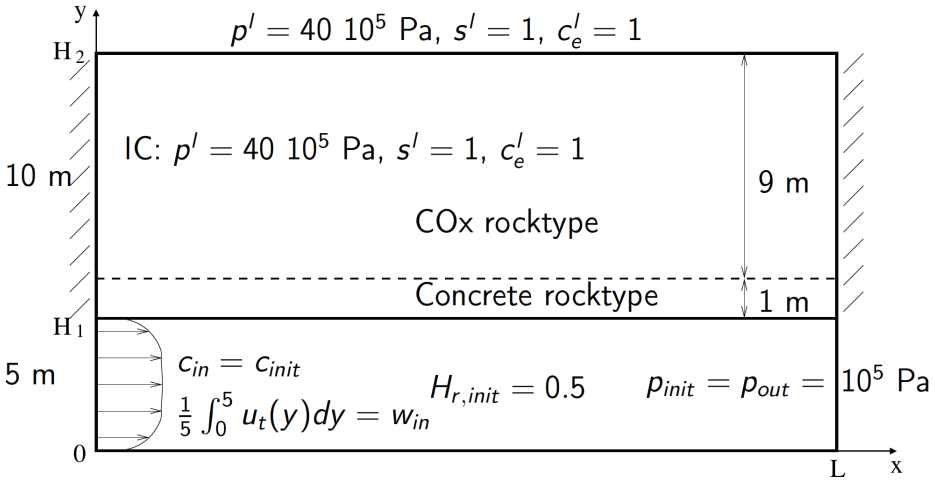

Figure 3: Setting of the Andra test case with a horizontal gallery.

roughly computed from the solution c_e of the stationary convection-diffusion equation in the gallery

$$\begin{cases} \operatorname{div}\Big(\mathbf{u}_t c_e - (D^g + D_t)\nabla c_e\Big) = 0 & \text{on } \Omega^g, \\ c_e = \frac{P_{sat}(T_e)}{p_{\text{out}}} & \text{on } \Gamma, \\ c_e = c_{\text{in}} & \text{on } \Gamma^g_{\text{in}}, \\ \nabla c_e \cdot \mathbf{n} = 0 & \text{on } \Gamma^g_{\text{out}} \cup \Gamma^g_N. \end{cases} \tag{18}$$

which roughly corresponds to the value observed in Figure 6 away from a short transient state. Once the porous medium is sufficiently dried at the interface, the water influx starts to decrease down to a much lower stationary state (case of a top boundary bringing water in the porous medium). This decreasing phase corresponds to the second stage of the drying process. Similarly, as shown in Figure 6, after a rapid transient increase, the relative humidity in the gallery is roughly constant during the first stage with a value which can be computed from the solution c_e of (18). Then, it decreases down to a stationary state during the second stage. These two stages of the simulation and the final stationary state can also be observed in Figure 5 which shows at different times the gas saturation in the porous medium and the water molar fraction in the gallery. Figure 6 exhibits the good convergence in space of the relative humidity in the gallery and of the mean evaporation rate at the interface. Table 1 shows the numerical behavior of the full simulations for various choices of the length of the gallery L and of the input velocity w_{in} and for the four meshes. We can observe a good scalability of the Newton and Quasi-Newton non-linear solvers and a good convergence of the fixed point iterations with roughly two or three fixed point iterations by time step. Figure 10 clearly shows that the solutions of the sequential algorithm, obtained with a single fixed point iteration, and of the converged fixed point algorithm can hardly be distinguished.

Finally, Figures 7-9 exhibit the comparison of the relative humidity in the gallery and of the evaporation rate at the interface obtained for the 2D-2D and for the reduced 2D-1D models with various values of the length L and of the input velocity w_{in}. It is clear that the larger the length the better the approximation of the relative humidity in the gallery provided by the reduced model. The approximation of the evaporation rate provided by the reduced model is good independently on the length of the gallery (away from a very short transient state) since it is only related to the diagonal approximation of the Steklov-Poincaré operator. In all cases, the reduced model provides a good order of magnitude of all quantities of interest.

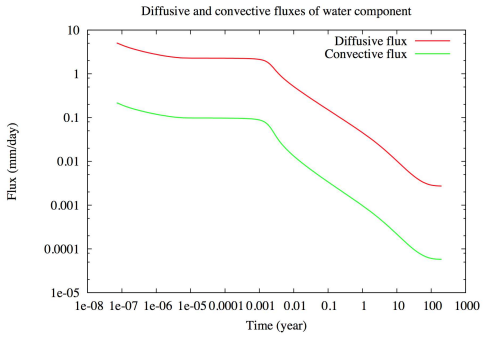

Figure 4: Mean diffusion and convection fluxes of the water component at the interface as a function of time with $L = 100$ m, $w_{\text{in}} = 0.5$ m.s^{-1} and the mesh 100×200.

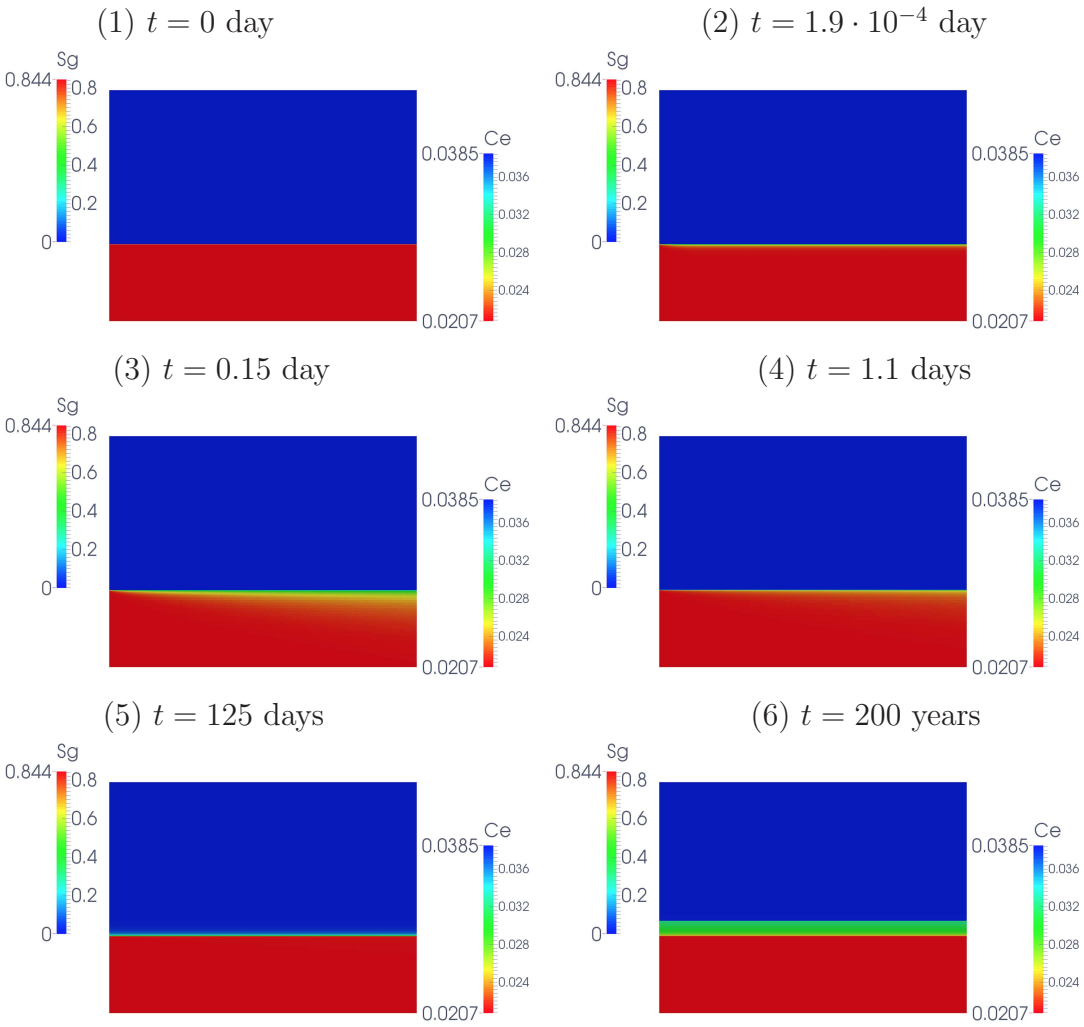

Figure 5: Gas saturation in the porous medium and water molar fraction in the gallery at different times with $L = 100$ m, $w_{\text{in}} = 0.5$ m.s^{-1} and the mesh 100×200.

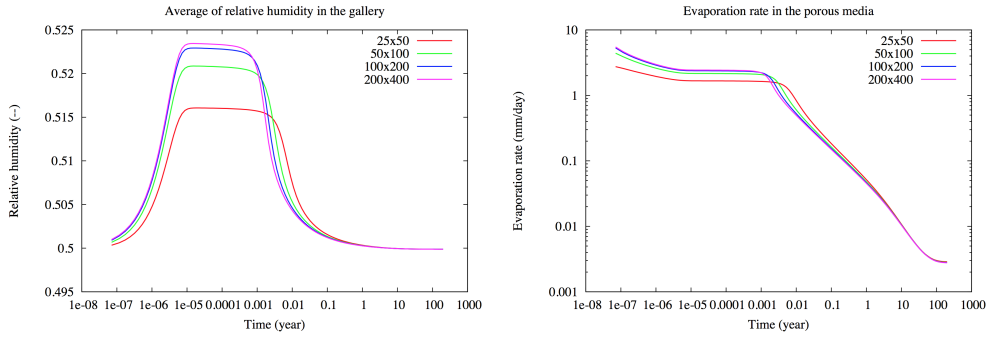

Figure 6: For each mesh and for $L = 100$ m, $w_{\text{in}} = 0.5$ m.s^{-1}: average of the relative humidity in the gallery (left) and evaporation rate at the interface (right) as a function of time.

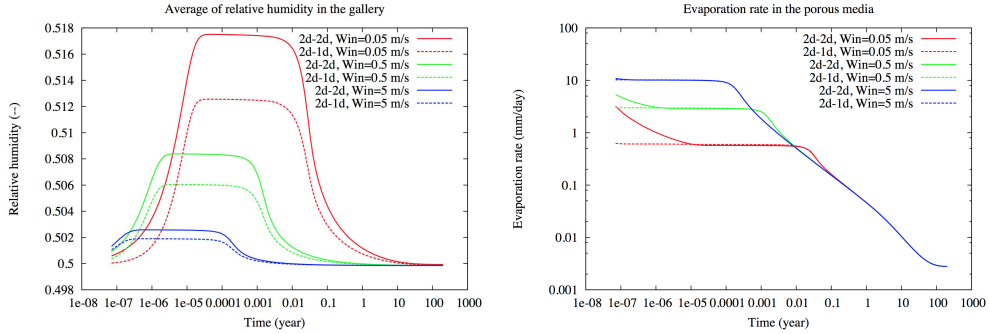

Figure 7: Comparison of the solutions obtained by the 2D-2D and 2D-1D models with $L = 25$ m and the mesh 100×200: average of relative humidity in the gallery (left), evaporation rate at the interface (right) as a function of time.

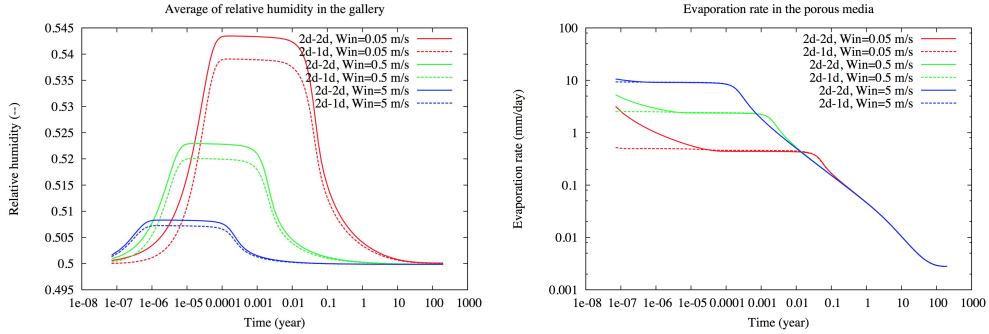

Figure 8: Comparison of the solutions obtained by the 2D-2D and 2D-1D models with $L = 100$ m and the mesh 100×200: average of the relative humidity in the gallery (left), evaporation rate at the interface (right) as a function of time.

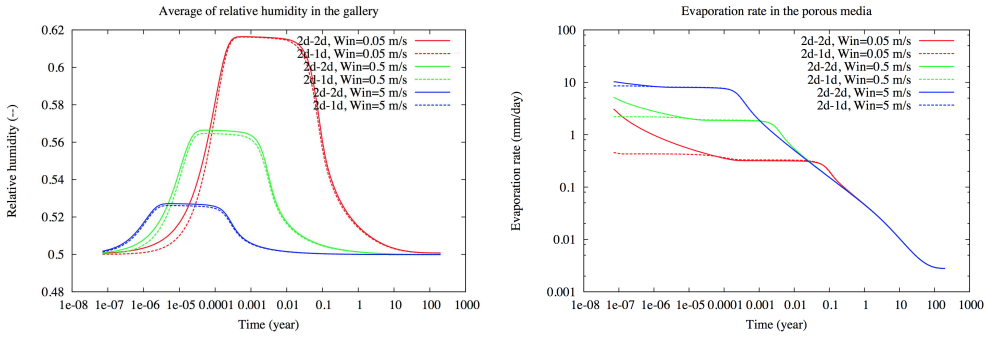

Figure 9: Comparison of the solutions obtained by the 2D-2D and 2D-1D models with $L = 400$ m and the mesh 100×200: average of the relative humidity in the gallery (left), evaporation rate at the interface (right) as a function of time.

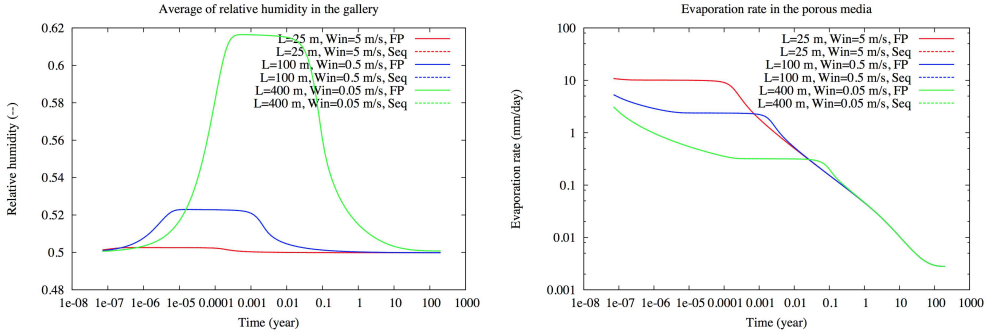

Figure 10: Comparison of the solutions obtained by the fixed-point (FP) and sequential (Seq) algorithms with the mesh 100×200: average of the relative humidity in the gallery (left), evaporation rate at the interface (right) as a function of time.

meshes	$N_{\Delta t}$	N_{Chop}	N_{Newton}	N_{Pt}	N_{NVS}	CPU (s)
25×50	123	0	504	239	435	7.56
50×100	123	0	527	257	480	48.64
100×200	123	0	552	277	525	388.47
200×400	123	0	582	287	552	3279.18
meshes	$N_{\Delta t}$	N_{Chop}	N_{Newton}	N_{Pt}	N_{NVS}	CPU (s)
25×50	123	0	591	305	590	8.60
50×100	123	0	636	315	615	58.86
100×200	123	0	690	324	634	486.11
200×400	123	0	753	343	661	4505.81
meshes	$N_{\Delta t}$	N_{Chop}	N_{Newton}	N_{Pt}	N_{NVS}	CPU (s)
25×50	123	0	673	349	694	9.89
50×100	123	0	792	368	726	73.12
100×200	123	0	864	383	778	620.51
200×400	123	0	923	388	786	7262.62

Table 1: For $(L, w_{\text{in}}) = (25, 5)$ (above), $(100, 0.5)$ (middle) and $(400, 0.05)$ (below) in m for L and m.s^{-1} for w_{in}, for each mesh, and for the full 200 years of simulation: number $N_{\Delta t}$ of successful time steps, number N_{Chop} of time step chops, number N_{Newton} of Newton iterations, number N_{Pt} of fixed point iterations, number N_{NVS} of Quasi-Newton iterations, CPU time in seconds.

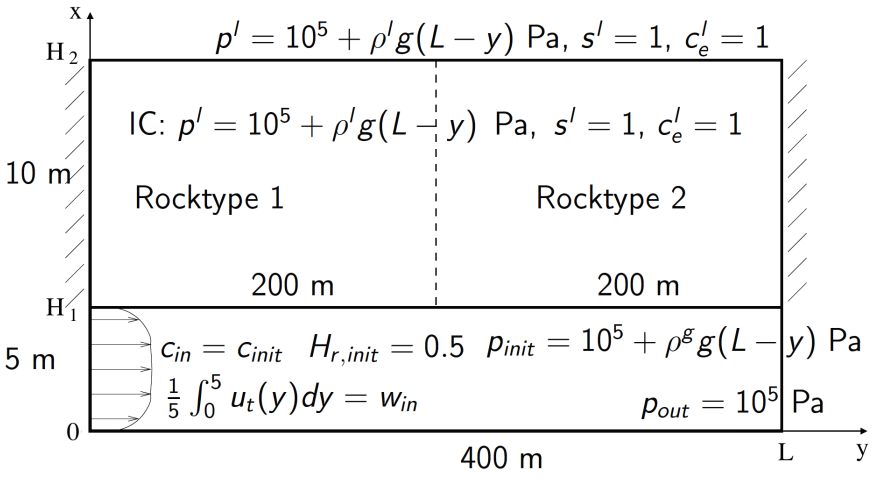

Figure 11: Setting of the Andra test case with a vertical gallery.

4.3 Andra test case with a vertical gallery

We consider in this test case a vertical gallery of length $L = 400$ m exhibited in Figure 11 (rotated of 90 degrees clockwise). The gallery is now defined by $\Omega^g = (0, H_1) \times (0, L)$ with $H_1 = 5$ m, and the porous medium by $\Omega^p = (H_1, H_2) \times (0, L)$ with $H_2 = 15$ m. The first rocktype for $y \leq 200$ m is defined by the parameters of the COx rocktype of the previous test case. The second rocktype is like the COx rocktype except that the permeability is larger by a factor 100.

The objectives of this test case are the following. Since the duration of the constant evaporation rate stage depends on the permeability, this test case with two different permeabilities along the direction of the gallery should exhibit a non constant evaporation rate even during the first stage of the drying process. Another consequence is that the assumption of a roughly constant water molar fraction along the direction of the gallery which is used to compute the boundary layer thickness of the reduced model should no longer be valid even during the first stage of the drying process. Hence it is a good test case to challenge the reduced 2D-1D model. The simulation is run over a period of 50 years with an initial time step of 1 s and a maximum time step of 10 years. The numerical solutions are obtained with the meshes $N_y \times N_x = 25 \times 73$, 50×143, 100×283, which are refined on both sides of the interface Γ as in the previous test case.

Figure 13 shows as expected that the evaporation rate and the relative humidity are no longer constant during the first stage of the drying process due to the heterogeneity of the permeability along the gallery. Figure 12 also clearly shows the influence of the two different permeabilities along the gallery on the evaporation rate and on the desaturation of the porous medium. We see that the desaturation front propagates at different time scales in the two rocktype regions. Figure 14 still exhibits a good match between the 2D-2D and the reduced 2D-1D models. However, as expected, it is not as good as in the previous test case. Figure 15 exhibits as previously that the solutions of the sequential and converged fixed point algorithms are basically the same. Table 2 exhibits, as in the previous test case, the good numerical behavior and scalability of the non-linear solvers.

4.4 Drying test case

In this test case exhibited in Figure 16, we consider the drying by convection of a homogeneous porous medium $\Omega^p = (0, L) \times (H_1, H_2)$ with $L = 1$ m, $H_1 = 0.5$ m, $H_2 = 1.5$ m. The Porous medium is assumed to be closed at the lateral boundaries Γ_N^p and at the top boundary Γ_D^p. The

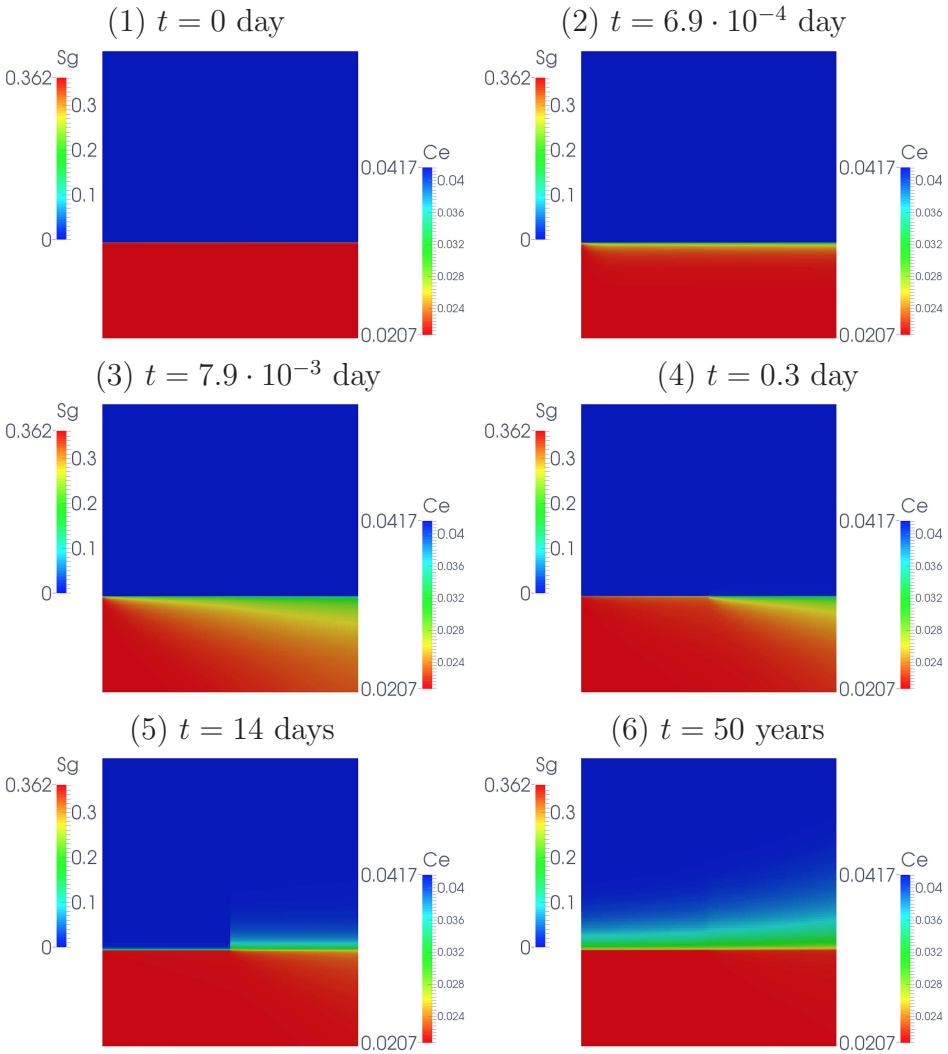

Figure 12: Gas saturation in the porous medium and water molar fraction in the gallery at different times with $w_{\text{in}} = 0.5$ m.s^{-1} and the mesh 100×283.

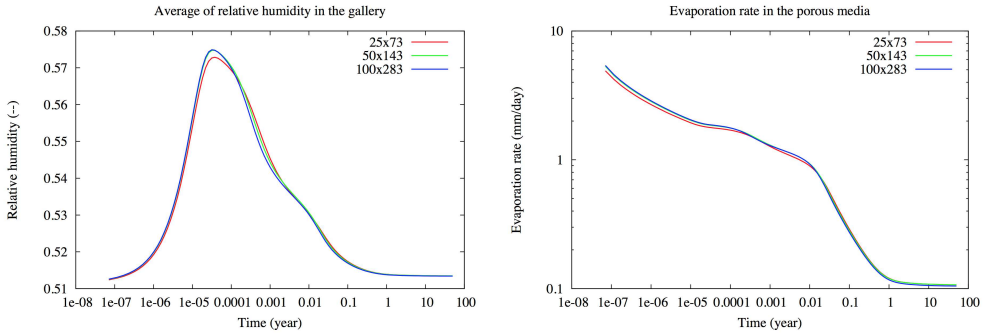

Figure 13: For each mesh and for $w_{\text{in}} = 0.5$ m.s^{-1}: average of the relative humidity in the gallery (left) and evaporation rate at the interface (right) as a function of time.

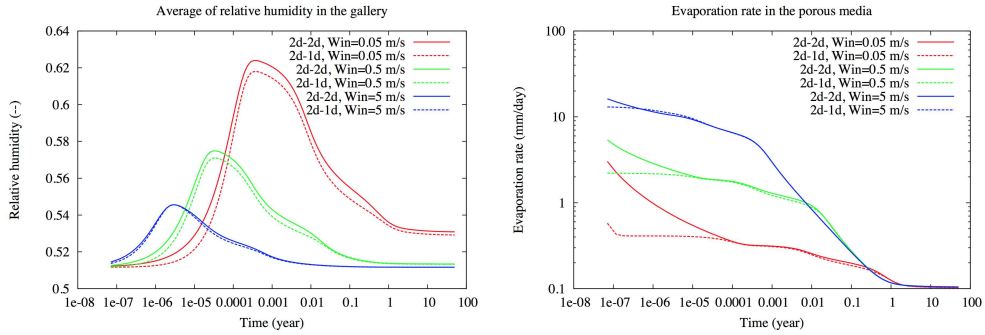

Figure 14: Comparison of the solutions obtained by the 2D-2D and 2D-1D models with the mesh 100×283: average of the relative humidity in the gallery (left), evaporation rate at the interface (right) as a function of time.

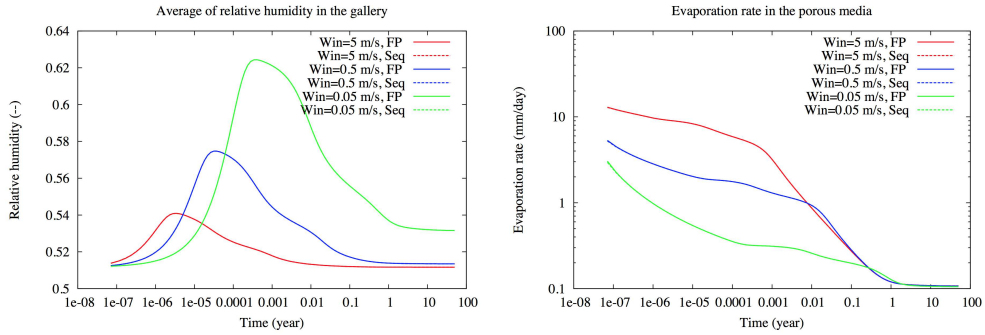

Figure 15: Comparison of the solutions obtained by the fixed-point (FP) and sequential (Seq) algorithms with the mesh 50×143: average of the relative humidity in the gallery (left), evaporation rate at the interface (right) as a function of time.

meshes	$N_{\Delta t}$	N_{Chop}	N_{Newton}	N_{Pt}	N_{NVS}	CPU (s)
25×73	108	0	882	397	765	18.57
50×143	108	0	963	406	805	123.43
100×283	108	0	1054	407	810	1155.48
meshes	$N_{\Delta t}$	N_{Chop}	N_{Newton}	N_{Pt}	N_{NVS}	CPU (s)
25×73	108	0	759	328	619	15.63
50×143	108	0	857	359	662	106.65
100×283	108	0	960	362	685	936.90
meshes	$N_{\Delta t}$	N_{Chop}	N_{Newton}	N_{Pt}	N_{NVS}	CPU (s)
25×73	108	0	595	278	539	12.59
50×143	108	0	648	278	540	85.77
100×283	108	0	706	288	551	760.54

Table 2: For $w_{\text{in}} = 0.05$ (above), 0.5 (middle) and 5 (below) in m.s^{-1}, for each mesh, and for the full 50 years of simulation: number $N_{\Delta t}$ of successful time steps, number N_{Chop} of time step chops, number N_{Newton} of Newton iterations, number N_{Pt} of fixed point iterations, number N_{NVS} of quasi-newton iterations, CPU time in seconds.

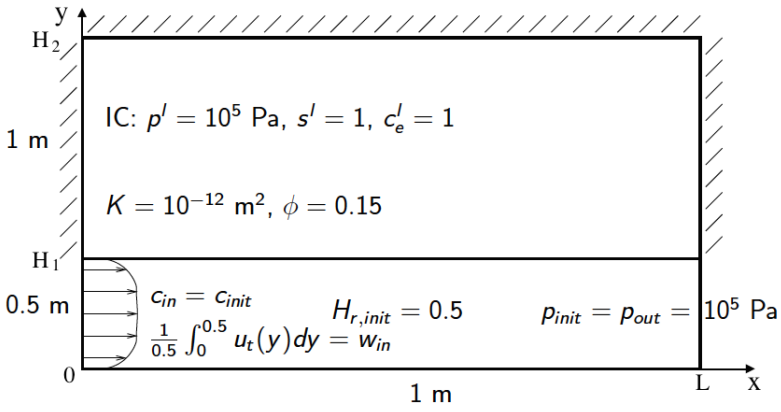

Figure 16: Setting of the drying test case.

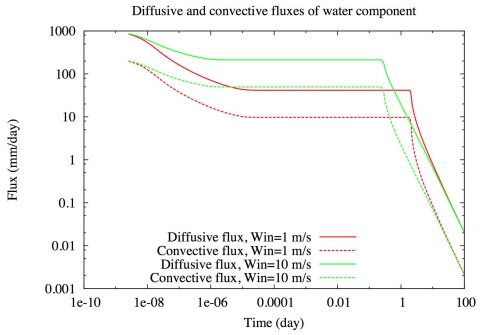

Figure 17: Mean diffusion and convection fluxes of water component at the interface as a function of time with the mesh 100×283.

rocktype is defined by the van Genuchten parameters $n = 4$, $s_r^l = s_r^g = 0$, $P_r = 15 \cdot 10^3$ Pa, the isotropic permeability $\mathbf{K} = 10^{-12}$ m^2 and the porosity $\phi = 0.15$. The temperature is fixed to a rather high value $T_e = 333$ K in order to increase the liquid evaporation rate. Consequently the water molar fraction at a relative humidity equal to 1 is not small any more and the water convection flux at the interface is not negligible anymore compared with the water diffusion flux. as exhibited in Figure 17. Note also that in this test case, the buoyancy forces in the porous medium are not small any more compared with the capillary forces as it was the case for the horizontal Andra test case. Therefore, the gas which penetrates in the porous medium rises up to the closed top boundary as shown in Figure 18. The simulation is run over a period of 100 days with an initial time step of 10^{-4} s and a maximum time step of 1 day. The numerical solutions are obtained with the meshes $N_x \times N_y = 25 \times 73$, 50×143, 100×283, which are, as for the first test case, refined on both sides of the interface Γ. The number of cells is roughly the same in both subdomains Ω^g and Ω^p.

The comparison of the 2D-2D and reduced 2D-1D models exhibited in Figure 20 shows not such a good match for the relative humidity. This is due to the fact that the 1D flow assumption in the gallery is no longer justified. On the other hand, the evaporation rate and the gas volume still exhibit a good match. This shows that the approximation provided by the boundary layer thickness model is still good.

Figure 19 shows that the spatial convergence is almost achieved for the coarsest mesh due to the strong refinement at the interface Γ. Figure 21 exhibits as before that the sequential algorithm provides basically the same accuracy than the converged fixed point algorithm. The numerical behavior given by Table 3 is still good.

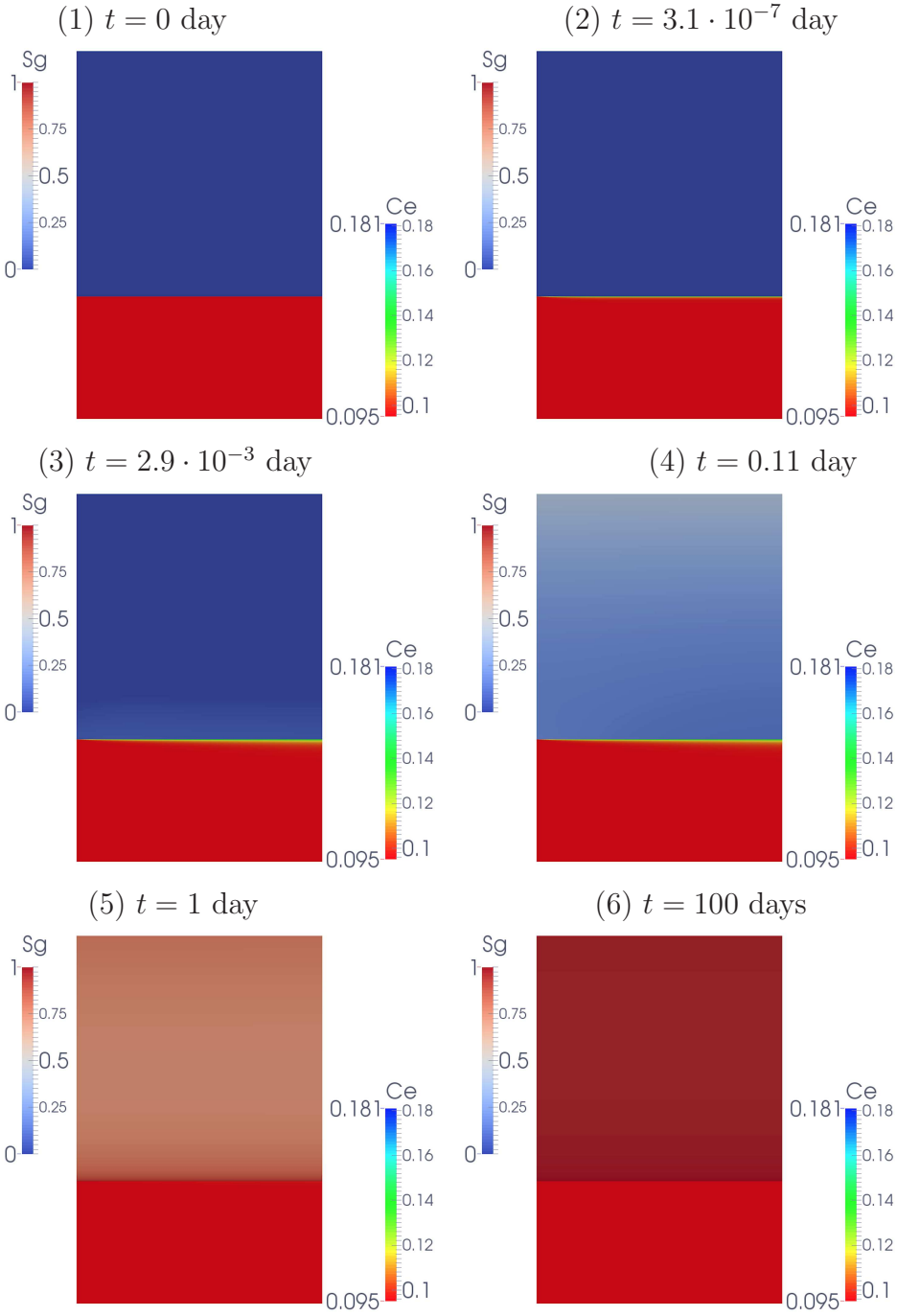

Figure 18: Gas saturation in the porous medium and water molar fraction in the gallery at different times with $w_{\text{in}} = 10$ m.s^{-1} and the mesh 100×283.

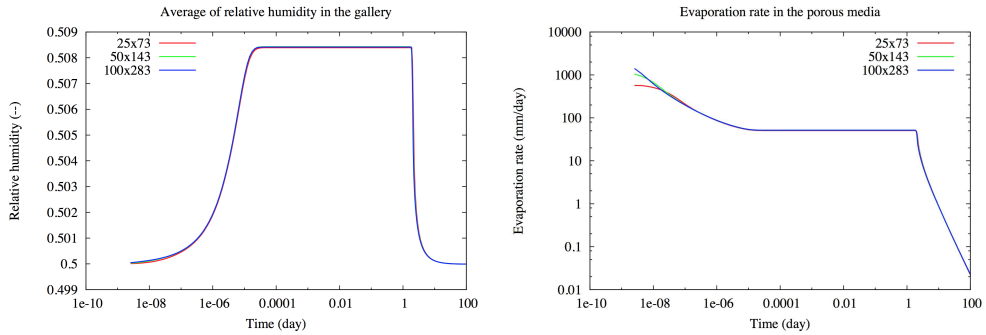

Figure 19: For each mesh and for $w_{\text{in}} = 1$ m.s^{-1}: average of the relative humidity in the gallery (left) and evaporation rate at the interface (right) as a function of time.

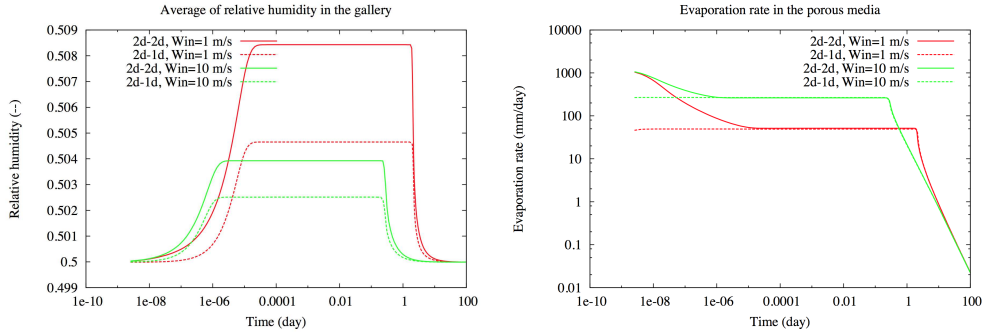

Figure 20: Comparison of the solutions obtained by the 2D-2D and 2D-1D models with the mesh 50×143: average of the relative humidity in the gallery (left), evaporation rate at the interface (right) as a function of time.

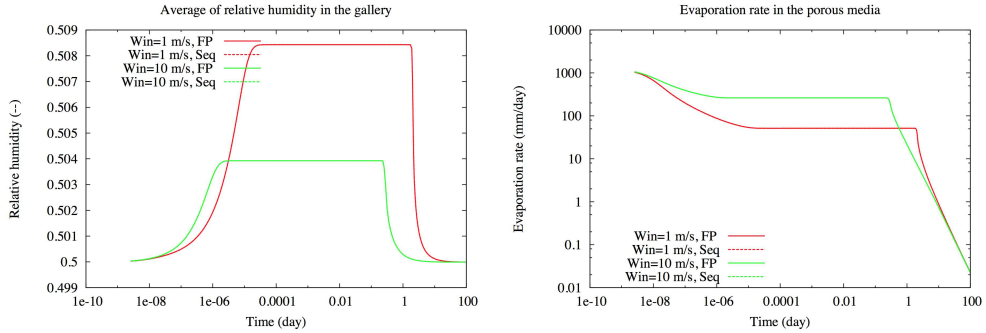

Figure 21: Comparison of the solutions obtained by the fixed-point (FP) and sequential (Seq) algorithms with the mesh 50×143: average of the relative humidity in the gallery (left), evaporation rate at the interface (right) as a function of time.

meshes	$N_{\Delta t}$	N_{Chop}	N_{Newton}	N_{Pt}	N_{NVS}	CPU (s)
25×73	215	2	1879	625	1265	38.00
50×143	218	3	2767	675	1390	334.00
100×283	233	7	4458	752	1562	4251.28
meshes	$N_{\Delta t}$	N_{Chop}	N_{Newton}	N_{Pt}	N_{NVS}	CPU (s)
25×73	208	0	1446	551	1017	30.47
50×143	212	1	2233	593	1104	271.19
100×283	223	4	3561	643	1183	3485.42

Table 3: For $w_{\text{in}} = 1$ (above) and 10 (below) in m.s^{-1} , for each mesh, , and for the full 100 days of simulation: number $N_{\Delta t}$ of successful time steps, number N_{Chop} of time step chops, number N_{Newton} of Newton iterations, number N_{Pt} of fixed point iterations, number N_{NVS} of quasi-newton iterations, CPU time in seconds.

5 Conclusions

In this article, a splitting algorithm has been introduced to solve the problem of coupling a liquid gas Darcy flow in a porous medium and a free gas flow. It can be used either as a fixed point or sequential algorithm. Our splitting is chosen in order to preserve the strong coupling between the water molar fraction in the free-flow domain and the liquid pressure and liquid flux at the interface, while it relaxes the weak coupling between the porous medium and the velocity and pressure in the free-flow domain. A good convergence of this fixed point algorithm has been observed on Andra and drying test cases in a simple 2D geometrical setting. This algorithm has the advantage compared with fully coupled approaches [3, 17, 23] to lead to the non-linear and linear solutions of simpler sub-systems. It also allows large time steps at the time scale of the porous medium as opposed to usual sequential algorithms [12, 10] for which the time steps are limited by the time scale of the free gas flow.

This model is compared with a reduced model using a 1D model in the free-flow domain. This reduced model uses an approximation of the gas molar fraction boundary layer thickness based on a low-frequency approximation of a Steklov-Poincaré operator. The comparisons performed on the 2D test cases show a good match of the evaporation rate. They also exhibit a good match of the relative humidity in the gallery for high ratios between the length and the diameter of the gallery.

References

[1] O. Angelini, C. Chavant, E. Chénier, R. Eymard and S. Granet, Finite volume approximation of a diffusion-dissolution model and application to nuclear waste storage, Mathematics and Computers in Simulation, 81 (10) (2011), pp. 2001-2017

[2] K. Aziz and A. Settari, Petroleum Reservoir Simulation, Applied Science Publishers (1979)

[3] K. Baber, K. Mosthaf, B. Flemisch, R. Helmig and S. Müthing, Numerical scheme for coupling two-phase compositional porous-media flow and one-phase compositional free flow, IMA Journal of Applied Mathematics, 77 (6) (2012)

[4] G.S. Beavers and D.D. Joseph, Boundary conditions at a naturally permeable wall, Journal of Fluid Mechanics, 30 (1967), pp. 197-207

[5] R.B. Bird, W.E. Stewart and E.N. Lightfoot, Transport phenomena, John Wiley and Sons (2007)

[6] K. Brenner, R. Masson, L. Trenty and Y. Zhang, Coupling of a two phase gas liquid compositional 3D Darcy flow with a 1D compositional free gas flow, ESAIM, Mathematical Modelling and Numerical Analysis, accepted in november 2015, http://dx.doi.org/10.1051/m2an/2015091.

[7] P. Chassaing, Turbulence en Mécanique des Fluides: analyse du phénomène en vue de sa modélisation à l'usage de l'ingénieur, Cépaduès- Editions (2000)

[8] K.H. Coats, An equation of state compositional model, SPE Reservoir Simulation Symposium Journal (1980), pp. 363-376

[9] K.H. Coats, Implicit compositional simulation of single-porosity and dual-porosity reservoirs, SPE Symposium on Reservoir Simulation (1989)

[10] T. Defraeye, Convective heat and mass transfer at exterior building surfaces, PhD thesis, Catholic University of Leuven, Leuven, Belgium (2011)

[11] T. Defraeye, Advanced computational modelling of drying processes - a review, Applied Energy, 131 (2014), pp. 323-344

[12] T. Defraeye, B. Blocken and J. Carmeliet, Analysis of convective heat and mass transfer coefficients for convective drying of a porous flat plate by conjugate modelling, Int. J. of Heat and Mass Transfer, 55 (2012), pp. 112-124

[13] J.W. Demmel, S.C. Eisenstat, J.R. Gilbert, X.S. Li and J.W.H. Liu, A supernodal approach to sparse partial pivoting, SIAM J. Matrix Analysis and Applications, 20 (3) (1999), pp. 720-755

[14] M. Discacciati, E. Miglio and A. Quarteroni, Mathematical and numerical models for coupling surface and groundwater flows, Appl. Num. Math., 43 (2002)

[15] V. Girault and B. Rivière, DG approximation of coupled Navier-Stokes and Darcy equations by Beaver-Joseph-Saffman interface condition, SIAM J. Numerical Analysis, 47 (2009)

[16] F. Harlow and J. Welch, Numerical calculation of time-dependent viscous incompressible flow of fluid with a free surface, Physics of Fluids, 8 (1965), pp. 2182-2189

[17] R. Helmig, B. Flemisch, M. Wolff, A. Ebigbo and H. Class, Model coupling for multiphase flow in porous media, Advances in Water Resources, 51 (2013)

[18] C. Japhet, F. Nataf and F. Rogier, The Optimized Order 2 Method. Application to Convection-Diffusion Problems, Future generation computer systems, 18 (1) (2001), pp. 17-30

[19] A. Lauser, C. Hager, R. Helmig and B. Wohlmuth, A new approach for phase transitions in miscible multi-phase flow in porous media, Advances in Water Resources, 34 (2011), pp. 957-966

[20] X.S. Li, J.W. Demmel, J.R. Gilbert, L. Grigori, M. Shao and I. Yamazaki, Technical report LBNL-44289, Lawrence Berkeley National Laboratory, SuperLU Users' Guide, September (1999), http://crd.lbl.gov/~xiaoye/SuperLU.

[21] J.-M. Masella, Q.H. Tran, D. Ferre and C. Pauchon, Transient Simulation of Two-Phase Flows in Pipes, Oil & Gas Science and Technology, 53 (6) (1998), pp. 801-811

[22] R. Masson, L. Trenty and Y. Zhang, Formulation of two phase gas liquid compositional Darcy flows with phase transitions, International Journal of Finite Volume, 11 (2014)

[23] K. Mosthaf, Modeling and Analysis of Coupled Porous-Medium and Free Flow with Application to Evaporation Processes, PhD thesis, University of Stuttgart (2013)

[24] K. Mosthaf, K. Baber, B. Flemisch, R. Helmig, A. Leijnse, I. Rybak and B. Wohlmuth, A coupling concept for two-phase compositional porous-medium and single-phase compositional free flow, Water Resources Research, 47 (10) (2011)

[25] S. Patankar, Numerical heat transfer and fluid flow, Series in Computational Methods in Mechanics and Thermal Sciences, XIII, Washington-New York-London: Hemisphere Publishing Corporation; New York. McGraw-Hill Book Company (1980)

[26] D.W. Peaceman, Fundamentals of Numerical Reservoir Simulations, Elsevier (1977)

[27] I. Rybak, J. Magiera, R. Helmig, C. Rohde, Multirate time integration for coupled saturated/unsaturated porous medium and free flow systems, Computational Geosciences, 19 (2015), pp. 299-309

[28] Y. Saad, Iterative Methods for Sparse Linear Systems, 2nd edition, SIAM, Philadelphia, PA (2003)

[29] Y. Saad, `http://www-users.cs.umn.edu/~saad/software/`

[30] O. Thual, Hydrodynamique de l'environnement, éditions de l'Ecole polytechnique (2010)

[31] P. Wesseling, Principles of Computational Fluid Dynamics, Springer (2001)

[32] Y. Zhang, Modélisation et simulation des dispositifs de ventilation dans les stockages de déchets radioactifs, PhD thesis, University Nice Sophia Antipolis, December (2015)